Journal of Pathology
J Pathol June 2023; **260:** 203–221
Published online 31 March 2023 in Wiley Online Library
(wileyonlinelibrary.com) **DOI:** 10.1002/path.6076

ORIGINAL ARTICLE

Novel prognostication biomarker adipophilin reveals a metabolic shift in uveal melanoma and new therapeutic opportunities

Maisoon Matareed[1†], Eleftheria Maranou[2,3†], Saara A Koskela[2,3], Arfa Mehmood[2], Helen Kalirai[1,2], Sarah E Coupland[1,2,3‡] and Carlos R Figueiredo[1,2,3*‡]

[1] *Liverpool Ocular Oncology Research Group (LOORG), Institute of Systems Molecular and Integrative Biology, Department of Molecular and Clinical Cancer Medicine, University of Liverpool, Liverpool, UK*
[2] *Medical Immune Oncology Research Group (MIORG), Institute of Biomedicine, Faculty of Medicine, University of Turku, Turku, Finland*
[3] *InFLAMES Research Flagship Center, University of Turku, Turku, Finland*

**Correspondence to: CR Figueiredo, Institute of Biomedicine, Faculty of Medicine, University of Turku, Turku, Finland. E-mail: crdefi@utu.fi*

[†]Equal contributions.
[‡]Equal contributions.

Abstract

Metastatic uveal melanoma remains incurable at present. We previously demonstrated that loss of *BAP1* gene expression in tumour cells triggers molecular mechanisms of immunosuppression in the tumour microenvironment (TME) of metastatic uveal melanoma. Adipophilin is a structural protein of lipid droplets involved in fat storage within mammalian cells, and its expression has been identified in uveal melanoma. We comprehensively evaluated adipophilin expression at the RNA (*PLIN2*) and protein levels of 80 patients of the GDC-TCGA-UM study and in a local cohort of 43 primary uveal melanoma samples respectively. *PLIN2* expression is a survival prognosticator biomarker in uveal melanoma. Loss of adipophilin expression is significantly associated with monosomy 3 status and nuclear BAP1 losses in uveal melanoma tumours. Integrative transcriptomic and secretome studies show a relationship between transient loss of adipophilin expression and increased levels of tumour-associated macrophages and hypoxia genes, suggesting *PLIN2*-dependent changes in oxygen and lipid metabolism in the TME of low and high-metastatic risk uveal melanoma. We designed four adipophilin-based multigene signatures for uveal melanoma prognostication using a transcriptomic and secretome survival-functional network approach. Adipophilin-based multigene signatures were validated in BAP1-positive and BAP1-negative uveal melanoma cell lines using a next-generation RNA sequencing approach. We identified existing small molecules, mostly adrenergic, retinoid, and glucocorticoid receptor agonists, MEK, and RAF inhibitors, with the potential to reverse this multigene signature expression in uveal melanoma. Some of these molecules were able to impact tumour cell viability, and carvedilol, an adrenergic receptor antagonist, restored *PLIN2* levels, mimicking the expression of normoxia/lipid storage signatures and reversing the expression of hypoxia/lipolysis signatures in co-cultures of uveal melanoma cells with human macrophages. These findings open up a new research line for understanding the lipid metabolic regulation of immune responses, with implications for therapeutic innovation in uveal melanoma.

Keywords: uveal melanoma prognostication; adipophilin; *BAP1* loss; immune suppression; drug discovery; adrenergic receptor antagonist; immunotherapy

Received 1 September 2022; Revised 2 January 2023; Accepted 22 February 2023

Conflict of interest statement: SEC is General Secretary of The Pathological Society of Great Britain and Ireland, the owner of this journal. No other conflicts of interest were declared.

INTRODUCTION

Uveal melanoma (UM) is the most aggressive intraocular tumour in adults. About 50% of UM patients will develop metastatic disease, typically in the liver, for which no treatments are available [1]. Immune checkpoint therapies achieved successful survival rates for metastatic cutaneous melanoma, although metastatic UM patients are unfortunately universally refractory to these treatments [2]. Thus, a better understanding of UM biology associated with existing risk factors can lead to the development of more effective treatments.

We have recently demonstrated that loss of the BRCA1-associated protein 1 gene (*BAP1*) in UM, regardless of the mutational load of this gene, is a core genetic transformation leading to immunosuppression of UM tumour microenvironment (TME), mainly coordinated by tumour-associated macrophages (TAMs)

[3,4]. Among the various TAM subsets [5], lipid-associated TAMs induce immunosuppression by canonical M2-like pathways using fatty acid (FA) metabolism [5] and are correlated with a worse survival outcome [6]. The impact of *BAP1* loss on cellular metabolism and immune functions has been described [7,8], suggesting that *BAP1* loss may modulate the immune TME of UM by governing metabolic routes that impact TAM biology. Indeed, reprogramming metabolism has been recognised as one of the hallmarks of the cancer [9], encompassing several mechanisms, including upregulated lipid metabolism and FA oxidation in the TME [10].

It has been suggested that BAP1-dependent control of lipid metabolism is associated with the upregulation of lipogenic pathways [11–13]. In primary UM (pUM), modified lipid metabolism was initially suggested after observing differences in the lipid droplet (LD) content in their TME using a LD marker called adipophilin (adipose differentiation-related protein, encoded by the gene *PLIN2*) [13]. Adipophilin is a critical structural protein responsible for developing, stabilising, and modifying LD. Adipophilin regulates cellular lipid metabolism by inhibiting LD dissociation and lipolysis [14–17], acquiring an important role in several metabolic diseases, including cancer [18].

Developing tailored metabolism-targeted approaches for *BAP1*-deficient UM is a current clinical need [19]. In this study, digital analysis of whole-slide images of pUM combined with their respective clinical data provided an expanded understanding of adipophilin-dependent lipid metabolism and its impact on patient survival. The study extends to a multi-omic analysis of UM metabolism using publicly available data from The Cancer Genome Atlas (TCGA)-UM study [20] and our local Liverpool Ocular Oncology Research Group (LOORG, Liverpool, UK) cohorts [3,21,22] to dissect the implications of adipophilin/*PLIN2* biology in UM metabolism. We identified new prognostic metabolic signatures for UM and specific small molecules currently in preclinical and clinical development that have the potential to reverse the expression profile of these signatures using an *in silico* approach for future functional evaluation. Understanding the metabolic heterogeneity of UM will help the optimal development of novel metabolism-targeting approaches for BAP1-negative secondary UM aiming to impact BAP1-induced changes in TME and patient survival.

Materials and methods

Cell lines

Human UM cell lines, Mel285 (RRID: CVCL_C303), were provided by (LOORG). MP46 (RRID:CVCL_4D13) were purchased from ATCC (MP46-CRL-3298, ATCC, Manassas, VA, USA). Mel285 was subcultured in RPMI-GlutaMAX (Gibco, Waltham, MA, USA), supplemented with 10% newborn calf serum (NBCS) (Gibco). MP46 was subcultured in RPMI-GlutaMAX (Gibco) supplemented with 20% NBCS and 1 mM sodium pyruvate (Gibco). Primary human macrophages were obtained from human peripheral blood monocytes as described previously [23].

Viability assay

Predicted anti-tumour drugs were purchased from commercial vendors. Stock solutions were prepared as follows: batimastat (Catalogue No. S7155, SelleckChem, Houston, TX, USA), bosutinib (Catalogue No. HY-10158/CS-0118, MedChemExpress, Monmouth Junction, NJ, USA), carvedilol (Catalogue No. HY-B0006/CS-1194), and palbociclib (Catalogue No. HY-50767A/CS-1327, MedChemExpress) were prepared as 10-mM stock solutions in DMSO. Fenbendazole (Catalogue No. HY- B0413/CS-2517, MedChemExpress), forskolin (Catalogue No. HY-15371/CS-1454, MedChemExpress), selumetinib (Catalogue No. HY-50706/CS-0059, MedChemExpress), tamibarotene (Catalogue No. HY-14652/CS-0654, MedChemExpress), and vemurafenib (Catalogue No. S1267, SelleckChem) were prepared as 50-mM stock solutions in DMSO. In brief, 1×10^4 Mel285 or MP46 cells were seeded into wells of 96-well plates and allowed to adhere for 4 h at 37 °C. Cells were incubated for 24 h with increasing concentrations ranging from 0 to 100 μM of bosutinib, carvedilol, and palbociclib, from 0 to 200 μM of batimastat, and from 0 500 μM of fenbendazole, forskolin, selumetinib, tamibarotene, and vemurafenib. Control wells were incubated with complete medium supplemented with corresponding tolerable concentrations of DMSO. After the incubation period, cell viability was determined using CellTiter 96 AQueous One Solution Cell Proliferation Assay (MTS; Promega, Madison, WI, USA) accordingly to the manufacturer's instructions. Absorbance was measured spectrophotometrically at 490 nm (Victor, PerkinElmer, Waltham, MA, USA). IC50 values were calculated from viability data using non-linear regression (Prism version 8.00, GraphPad Software, San Diego, CA, USA).

Ex vivo co-culture assay

Mel285 or MP46 cells were seeded in direct contact with human primary macrophages at a 1:4 ratio (8×10^4 cancer cells and 3.2×10^5 macrophages) in RPMI medium supplemented with 10% NBCS in a six-well plate, as described elsewhere [24]. Co-cultures were treated with half of the maximal inhibitory concentration (IC50) of carvedilol obtained from the viability assay. After a co-culture period of 24 h, all cells were harvested, and the RNA was isolated using the RNeasy Mini Kit (Qiagen, Germantown, MD, USA).

Reverse transcription–quantitative PCR (RT–qPCR)

Total RNA from co-cultures using human UM cells and macrophages was used for reverse transcription. cDNA was prepared from 1 μg RNA per sample, and qPCR was performed using iTaq Universal SYBR Green

Supermix (Bio-Rad, Hercules, CA, USA) and the CFX96 Touch Real-Time PCR Detection system (Bio-Rad). The primer sequences used to amplify the adipophilin-related transcriptomic signatures are listed in supplementary material, Table S4. Relative expression levels were normalised to *GAPDH* expression as previously described [25].

Next-generation RNA-sequencing

Total RNA from Mel285 and MP46 UM cells lines was isolated as mentioned earlier. The RNA quality and integrity were assessed, and the RNA integrity number (RIN) of the samples used in this study was ≥9. Total RNA (100 ng) was used for the Illumina Stranded mRNA Library preparation (Illumina, San Diego, CA, USA). RNA-seq was performed by the Finnish Functional Genomics Centre (FFGC, Turku Bioscience, Finland) using an Illumina NovaSeq platform. A paired-end 2 × 100 bp strategy was followed for each sample. The sequencing depth was 41 and 47 M reads per Mel285 and MP46 sample respectively. The quality of the sequenced reads was examined using FastQC (version 0.11.9) tool. Kallisto (version 0.48.0) was used to quantify the transcript per million (TPM) values using the human reference genome (GRCh38) [26]. The fold-change between the TPM values of the two cell lines was calculated using the following formula, and the heatmap was generated using the R pheatmap package: $GeneTPM_{Mel285}$-$GeneTPM_{MP46}$/$GeneTPM_{MP46}$.

Ethics statement and licenses

Access to human UM samples was granted by the Ocular Oncology Biobank (REC Ref21/NW/0139) under project-specific ethical approval from the Health Research Authority (REC Ref 15/SC/0611). Human peripheral blood was obtained from the Finnish Red Cross Blood Service (approval license: 16/2022).

Sample selection and preparation

pUM ($n = 43$) enucleation specimens were examined. The cases were selected according to tissue availability within the Liverpool Ocular Oncology Biobank with informed consent from the patients, who underwent the surgical procedure between 2016 and 2018 at the Liverpool Ocular Oncology Centre (LOOC) and Ethics Committee approval for the study (REC Ref 15/SC/0611). All cases were studied using conventional and immunohistochemical methods, as described previously [27], from the formalin-fixed paraffin-embedded (FFPE) blocks. Pseudo-anonymised clinical and genetic information was available (Table 1). Adipophilin protein levels were quantified by immunohistochemistry using an automated machine learning strategy, as previously described [25]. All samples were assessed for nuclear BAP1 expression (nBAP1) using the mouse anti-human BAP1 antibody (0.5 µg/ml; Catalogue No. sc-28383, clone: C-4, Santa Cruz, Insight Biotechnology Ltd, Middlesex, UK) and for adipophilin using rabbit anti-human adipophilin polyclonal antibody (Catalogue No. LS-B4850; 1:500; Lifespan Biosciences, Seattle, WA, USA) and further detected using the 3-Amino-9-ethyl carbazole peroxidase substrate (AEC) or 3,3'-diaminobenzidine (DAB) chromogens, as described previously [27]. Digital slide scanning was performed using an Aperio slide scanner (Aperio CS2) at ×20 magnification. Image files were extracted using Aperio Imagescope software.

Genetics and clinical information

The 43 pUM enucleations were from 24 male and 19 female patients. The median age of patients at diagnosis was 71 years (range 35–89). The tumours had a mean largest basal diameter (LBD) of 15.0 mm and a mean ultrasound height of 8.3 mm. Nineteen cases (38%) had ciliary body involvement, and 13 (26%) had extraocular spread. Epithelioid cells were present in 42% UM (Table 1). Multiplex ligation-dependent probe amplification (MLPA) and microsatellite analysis (MSA) provided the information on chromosomal alterations for all tumours in this study [28]. Thirty two pUM were classified as M3 (64%), 11 were classified as disomy 3 (D3) (22%), and 6 had partial loss of chromosome 3 (12%) (Table 1).

Machine learning digital analysis of full scanned images using NIS-Elements

The NIS-Elements Advanced Software (V4.20.23, Nikon, Melville, NY, USA) was used to customise the quantification of LD objects within digitally scanned slides as previously described [25,29–31]. In brief, regions of interest (ROI) were applied manually to select the tumour areas. ROIs with tissue deformation were excluded based on size, circularity, and signal intensity (chromogen interference, empty spaces). The automated measurement tool generated binary regions based on colour Hue, Intensity, and Saturation (HIS), or the combination of red, green, and blue (RGB) colours. Varying levels of endogenous brown melanin were present in some UM samples and were subtracted from unstained serial section control images to those cases stained with DAB chromogen. The areas of the total tumour ROI and the binary adipophilin stained zones were measured in pixels squared (px^2) and further converted to frequency, assuming ROI (whole tumour) to be 100% of the total studied area.

GDC-TCGA data analysis

Publicly available 80 pUM RNA-seq and clinical data [20] were extracted from the TCGA-UM study [20] using UCSC Xena browser 15 (available at http://xena.ucsc.edu/). RNA expression was presented using the Illumina HiSeq 2000 RNA sequencing platform version 2 and normalised by HTSeq/FPKM-UQ strategies. Data regarding *PLIN2* mRNA expression were derived along with age, *BAP1*, and chromosome 3 status.

Table 1. Clinicopathological characteristics of UM samples examined.

Histology number	Gender	Age (years)	Location of tumour	CBI	Chr3	Chr6p	Chr6q	Chr8p	Chr8q	Epithelioid cells	Adipophilin expression area (%)	Nuclear BAP1
1	M	72	Ciliary body	Yes	L	G	N	N	N	Yes	0.01	Negative
2	F	78	Ciliochoroid	Yes	L	N	N	N	G	Yes	0.09	Negative
3	M	74	Choroid	Yes	L	N	N	N	G	Yes	0.22	Negative
4	F	70	Choroid	No	L	N	N	N	N	Yes	0.58	Negative
5	M	80	Choroid	Yes	L	N	N	N	G	Yes	4.22	Negative
6	M	67	Ciliochoroid	No	L	N/E	N/E	N/E	N/E	No	0.28	Negative
7	M	72	Ciliochoroid	Yes	L	N/E	N/E	N/E	N/E	Yes	0.12	Negative
8	F	64	Choroid	No	L	N	N	N	G	Yes	6.22	Negative
9	F	74	Choroid	Yes	L	N	N	G	G	Yes	0.49	Negative
10	M	72	Choroid	No	L	N	N	G	G	No	1.04	Negative
11	F	69	Choroid	No	L	G	N	G	G	Yes	1.72	Negative
12	M	59	Choroid	No	L	N	N	G	G	Yes	3.49	Negative
13	F	69	Choroid	Yes	L	N	N	N	G	Yes	3.16	Negative
14	F	81	Choroid	No	L	G	N	L	G	Yes	3.96	Negative
15	M	69	Choroid	No	L	L	N	G	G	Yes	9.38	Negative
16	F	69	Choroid	Yes	L	N	N	L	G	Yes	1.70	Negative
17	F	82	Ciliochoroid	Yes	L	N	N	N	G	Yes	3.25	Negative
18	M	75	Choroid	Yes	L	N	N	G	G	Yes	6.08	Negative
19	M	63	Choroid	No	L	N	N	G	G	Yes	9.80	Negative
20	F	75	Choroid	Yes	L	G	N	G	G	Yes	6.31	Negative
21	M	77	Ciliary body	Yes	L	N	N	L	G	Yes	0.82	Negative
22	M	82	Ciliochoroid	Yes	L	N	N	N	G	Yes	6.99	Negative
23	F	55	Ciliochoroid	Yes	L	G	G	G	G	Yes	7.15	Negative
24	M	73	Choroid	No	L	N	N	N	G	Yes	11.33	Negative
25	F	45	Choroid	Yes	L	U	U	U	U	Yes	6.79	Negative
26	M	50	Ciliochoroid	Yes	L	G	N	N	G	Yes	12.11	Positive
27	M	72	Ciliochoroid	Yes	L	N	N	G	G	No	9.18	Positive
28	M	53	Ciliochoroid	No	L	N	N	N	N	Yes	8.61	Positive
29	F	72	Ciliochoroid	No	L	N/E	N/E	N/E	N/E	No	5.87	Positive
30	F	88	Choroid	No	N	G	N	G	N	No	3.80	Positive
31	F	58	Choroid	No	N	G	N	G	G	Yes	1.05	Positive
32	M	90	Choroid	No	N	N	N	N	N	No	8.65	Positive
33	M	62	Choroid	Yes	N	G	N	N	N	No	0.44	Positive
34	M	68	Choroid	Yes	N	G	N	N	N	No	0.23	Positive
35	F	80	Ciliochoroid	No	N	N	N	N	N	No	12.54	Positive
36	M	79	Choroid	No	N	G	L	N	G	No	0.11	Positive
37	M	68	Choroid	No	N	G	N	N	N	No	12.57	Positive
38	M	64	Choroid	No	N	N/E	N/E	N/E	N/E	No	15.54	Positive
39	F	35	Choroid	Yes	PL	G	N	N	G	No	9.76	Positive
40	F	75	Ciliochoroid	Yes	PL	N	N	N	N	No	8.78	Positive
41	F	72	Choroid	No	PL (L3p)	N	N	N	N	Yes	7.12	Positive
42	M	37	Ciliochoroid	No	PL (L3p)	G	N	N	N	No	6.99	Positive
43	M	84	Choroid	No	PL (L3p)	N	L	G	G	Yes	15.32	Positive

F, female; G, gain; L, loss; M, male; N, normal; N/E, not evaluated; PL, partial loss.

UM-Secretome analysis and GDC-TCGA-UM studies

UM-secretome data from UM samples were reviewed from a previous LOORG cohort [21]. The matrix of proteins with significant fold-change expression scores identified in the UM secretome is associated with the patient's risk of developing metastasis: High Risk (3), Low Risk (2) and no risk (normal, 1). The risk associated with each protein (protein Clinical Score) is calculated by the difference between the Highest and Lowest mean condition of the protein expressed in the cohort, resulting in four possible scores: no risk (−2), low risk (−1), mid risk (+1) and high risk (+2) (supplementary material, Table S1). Proteins were sorted accordingly to their fold-change expression levels in the secreted media. Further, the name of the proteins was converted into gene codes and uploaded in the GDC-TCGA-UM cohort-linked with XenaBrowser web-based analysis tool [3] to generate the cluster expression profile of these genes, supervised by *PLIN2*. The Kaplan Meier survival analysis of each gene was recovered from the GDC-TCGA-UM data bank. The log-rank, p values, and survival profile (good and poor survival prognosis) were included in a matrix (supplementary material, Table S3). Genes matching clinical scores from LOORG secretome data and TCGA-UM data were used for network plasticity analysis.

Tissue immunofluorescence

Antigen retrieval was performed on sections of FFPE tissues ($n = 12$ pUM) using the Dako PT Link system (Dako, Agilent Technologies LDA UK Limited,

Stockport, UK). Immunofluorescence was performed as described previously [25]. The following antibodies and reagents were used: anti-adipophilin polyclonal antibody (Catalogue No. LS-B4850; 1:500; Lifespan Biosciences) at 1:250, anti-CD163 at 1:400 (Catalogue No. NCL-L-CD163, clone: 10D6, Leica Microsystem [UK] Ltd, Milton Keynes, UK) and incubated with goat anti-rabbit Alexa Fluor 555 1:200 (red, Leica) and goat anti-mouse Alexa Fluor 488 1:200 (green, Leica) in addition to Hoechst 33342 (10 µg/ml) (Blue, ThermoFisher, Waltham, MA, USA).

Network and transcriptomic metabolic plasticity analysis

The genes related to normoxia, hypoxia, lipid metabolism, and lipolysis supervised by *BAP1* expression levels were individually analysed as a prognosticator marker in Kaplan–Meier curves at the Xena browser. The genes were marked as having good and poor prognoses based on their differential expression. The network plots of good and poor prognosis genes were generated using the *circlize* package in R [32]. The genes were associated with the hypoxia and lipid categories were collected from the literature and NanoString PanCan Immune Oncology multigene panel, as described previously [3]. The width of the links towards the hypoxia and lipid categories represents the variance of the gene in all the samples, which is calculated from the gene expression score obtained from the GDC-TCGA-UM cohort as previously described [32]. The links are coloured based on the log-rank *p*-value of the Kaplan–Meier curve.

L1000FWD drug prediction studies

The L1000FWD web-based application allows the query of gene expression signatures against signatures created from human cell lines treated with over 20,000 small molecules and drugs for the LINCS project [33]. The normalised RNA-seq data of identified multi-gene signatures supervised by *PLIN2* (Figure 4C and supplementary material, Table S3) was obtained from TCGA using the UCSC Xena Browser as previously described [3]. *PLIN2*-supervised multi-gene signatures were uploaded into the L1000FWD platform [33]. The drug signatures profile is shown in a scaffold network distribution where red clusters represent groups of drugs tested in different human cells with the potential to mimic the multi-gene signature that drives the metabolic shift in UM. Blue clusters represent the group of drugs with the highest potential to reverse the gene expression in the query.

Statistical analysis

Graphpad prism 5.0 software was used for statistical analysis. The Shapiro–Wilk normality test was performed for all group samples. Unpaired two-tailed Mann–Whitney *U*-test (non-parametric) was used to evaluate a significant difference between $CD163^{+}$adipophilin^{+} cells and nBAP1 stained groups. Non-parametric two-tailed Spearman's correlation studies between two variables were used. Xena-browser was used to generate all Kaplan–Meier survival plots. The log-rank test was used in UCSC Xena to evaluate the significance of survival curves providing χ^2 and p values. Differences were considered significant when $^{*}p < 0.05$, $^{**}p < 0.01$, $^{***}p < 0.001$ and $^{****}p < 0.0001$.

RESULTS

Adipophilin predicts survival and clinical outcome in pUM

Previous findings by our group reported the expression of adipophilin in a pUM cohort (Fiorentzis cohort, $n = 28$). We grouped the pathological estimation of adipophilin expression (intensity × proportion) of the Fiorentzis cohort into disomy 3 and monosomy 3 group status and observed that there is a decrease, but not significant, in adipophilin expression in monosomy 3 pUM compared with disomy 3 in this group cohort (supplementary material, Figure S1A). To evaluate if adipophilin expression is significantly reduced in monosomy 3 phenotype in a larger cohort, we initially revisited the GDC-TCGA-UM transcriptomic data for adipophilin gene expression (*PLIN2*). We examined the impact of differential expression of *PLIN2* on UM patient survival and *PLIN2* expression chromosome 3 copy number, *BAP1* levels, and age distribution. We observed that lower expression of *PLIN2* is significantly associated with poor UM patient survival (Figure 1A), monosomy 3 status and *BAP1* loss (patients with *BAP1* levels lower than the median of the gene expression) (Figure 1B). Interestingly, we observed that the older the patient, the lower the expression levels of *PLIN2* (Figure 1C). These clinical and genetic associations to adipophilin in the transcriptomic level (*PLIN2*) are in accordance with the ones observed in Fiorentzis cohort [13], showing for the first time a significant correlation between *PLIN2* downregulation with reduced survival, as well as its association with *BAP1* loss and monosomy 3 status and age.

Then, we evaluated adipophilin expression at the protein level in a second larger local UM cohort (LOORG, $n = 43$), including clinical data (Table 1). This second cohort was previously well-phenotyped for nBAP1 expression using immunohistochemistry and chromosome 3 copy number variation. Primary FFPE sections stained for adipophilin by immunohistochemistry were fully scanned, and adipophilin levels were measured by applying a high-precision machine learning method based on the circularity and size of particles of interest, as previously described [23,25]. Representative images of adipophilin developed with AEC red chromogen are shown, including NIS-Elements particle identification threshold from the entire tumour area are shown (blue for nBAP1 negative and red for nBAP1 positive tumours) (Figure 1D). Similar to the Fiorentzis and the GDC-TCGA-UM cohorts, adipophilin levels were

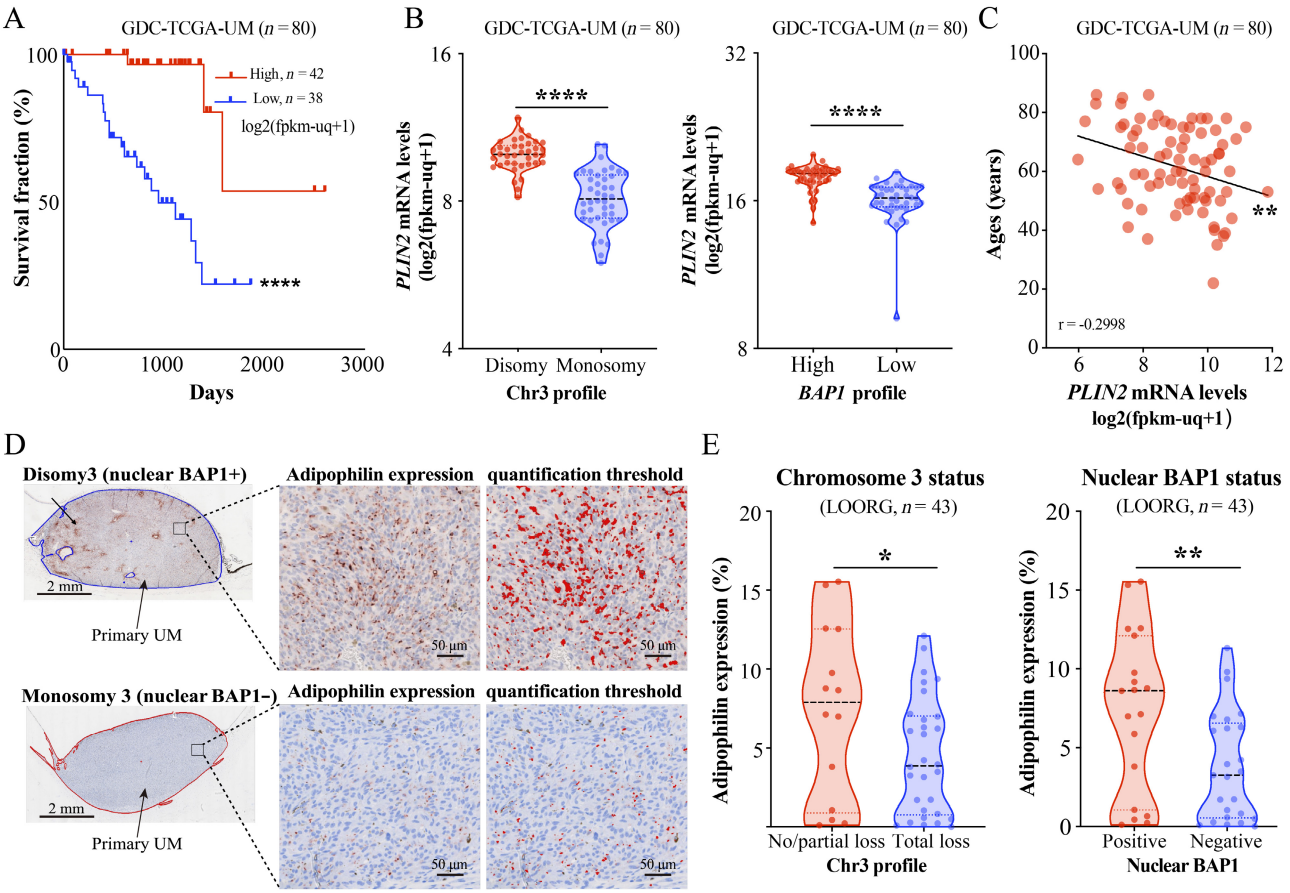

Figure 1. *PLIN2* mRNA expression levels are associated with survival and prognostication parameters in primary UM. (A) Kaplan–Meier survival curve sorted by *PLIN2* mRNA expression levels. *PLIN2* cutoff was determined by the best curve statistical fit in the GDC-TCGA-UM patient distribution cohort (****$p < 0.0001$, log-rank statistics = 18.95). (B) (Left) Differential expression of *PLIN2* mRNA among disomy 3 and monosomy 3 patients extracted from the GDC-TCGA-UM cohort ($n = 40$ patients for each group), two-tailed unpaired *t*-test (****$p < 0.0001$). (Right) Differential expression of *PLIN2* mRNA in groups of patients expressing high and low levels of *BAP1* in GDC-TCGA-UM cohort ($n = 40$ patients for each group), two-tailed unpaired *t*-test (****$p < 0.0001$), two-tailed unpaired *t*-test (****$p < 0.0001$). (C) Non-parametric two-tailed Spearman's correlation between age (years) and *PLIN2* mRNA levels in GDC-TCGA-UM cohort ($r = -0.29$, **$p = 0.006$). (D) Representative immunostaining for adipophilin detected with red chromogen (AEC) in nuclear BAP1-negative (–) and nuclear BAP1-positive (+) tumours. Enhanced images highlight the binary identification threshold in red for LD detected in the automated analysis performed in NIS-Elements software with guided cell circularity and size parameters. (E) Automated quantification of adipophilin frequency levels within total tumour area (corresponding to 100%) in disomy 3, monosomy 3 (left), and nuclear BAP1-positive and BAP1-negative groups (right) from 43 pUM tumours (LOORG cohort). Two-tailed *t*-test (*$p < 0.05$). Two-tailed, unpaired *t*-test (**$p < 0.01$).

reduced in the group of patients with monosomy 3 and nBAP1 negative status (Figure 1E).

Interestingly, we also found a negative correlation between adipophilin expression and patient age (supplementary material, Figure S1B). Whether this correlation is due to the tumour metabolic evolution or a normal ageing phenotype needs further evaluation in a larger RNA-seq cohort of normal eye tissues with similar age ranges, something that is currently not available. However, a preliminary analysis using the RNA-seq of the NIH Eye Integration cohort ($n = 8$) [34] shows that *PLIN2* levels are significantly higher in the retina of fetal eyes compared with the retina of adult eyes (supplementary material, Figure S1C), suggesting that the decrease of *PLIN2* expression might be affected by ageing, and may be a contributing factor to an increased cancer risk with advancing age [35].

The fact that this clinical phenotype is associated with adipophilin in both RNA and protein levels from two independent cohorts (LOORG and GDC-TCGA-UM) suggests that adipophilin levels may be directly controlled by *PLIN2* differential expression in UM. We did not observe a correlation between adipophilin expression and copy number variations in chromosomes 6p, 6q, 8p, and 8q (supplementary material, Figure S2A–D), nor with patients' tumour ciliary body extension (CBI), cell type, the occurrence of extraocular extension (EOE), gender, necrosis profile, tumour height, tumour LBD, and mitotic count (supplementary material, Figure S2E–L).

BAP1 and PLIN2 loss is associated with increased expression of HIF1A and macrophage levels in primary UM

Recent evidence shows that loss of *BAP1* expression impacts cell metabolism and immune functions [7,8]. Our recent findings on *BAP1* loss in UM as the main

contributing factor driving tumour immunosuppression in a TAM-dependent manner [3] suggest that *BAP1* loss, adipophilin (and, thus, lipid metabolism), and TAM levels are linked variables. First, we evaluated whether *CD163* as a macrophage gene marker could be associated with poor survival outcomes in the GDC-TCGA-UM cohort. We observed that the higher the expression of *CD163*, the lower the survival of UM patients (Figure 2A). Lipid consumption is one terminal metabolic feature of CD163$^+$ M2-like TAMs [5,36]. It is an alternative metabolic pathway during oxygen deprivation in cancer, mainly regulated by the expression of hypoxia-inducible factors (HIFs) such as HIF-1α (gene *HIF1A*) [37]. We observed that the lower the levels of *BAP1* in the GDC-TCGA-UM cohort, the higher the levels of *CD163* and *HIF1A* and the lower the expression of *PLIN2* lipid storage marker (red) (Figure 2B). Indeed, LDs containing adipophilin appear to be

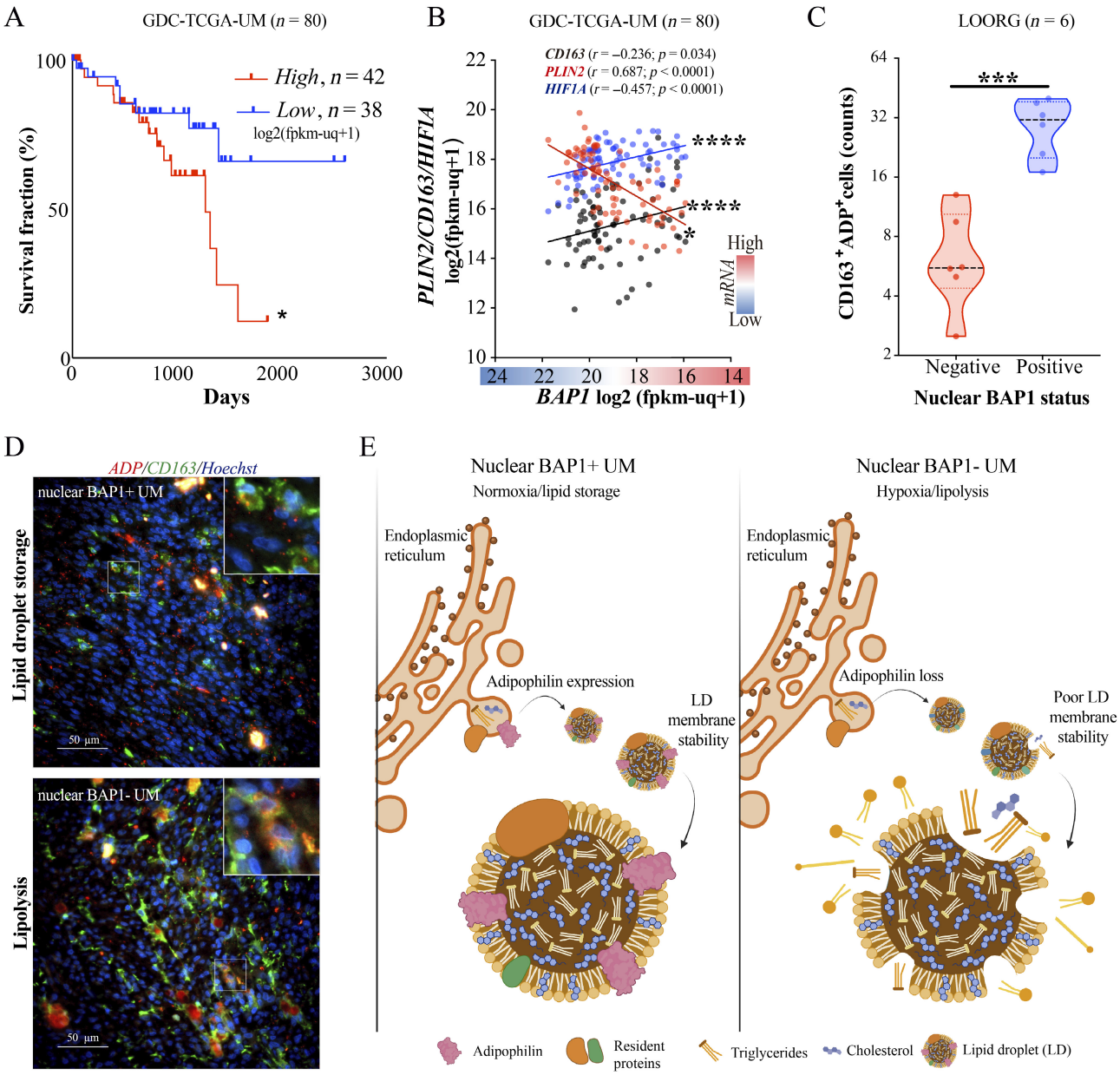

Figure 2. Adipophilin regulation is associated with an increase in TAMs and metabolic changes in pUM. (A) Kaplan–Meier survival curve sorted by *CD163* mRNA expression levels. *CD163* mRNA expression cutoff was determined in the same patient range adopted for *PLIN2* cutoff in the GDC-TCGA-UM cohort (****$p < 0.0001$, log-rank statistics = 18.95). (B) Spearman's multiple correlation analysis of sorted UM cases by *BAP1* loss (red-blue axis) and *PLIN2*, *CD163*, and *HIF1A* mRNA expression levels in the GDC-TCGA-UM cohort. Non-parametric two-tailed Spearman's rank correlation (*r*). (C) Quantifying adipophilin (ADP)+ LD counts in CD163$^+$ TAMs of UM primary samples with negative and positive nuclear BAP1 status. Two-tailed, unpaired *t*-test (***$p < 0.001$). (D) Tissue immunofluorescence (IF) for CD163 (green), nuclei (Hoechst, blue), and ADP (red) in nBAP1-negative (–) and nBAP1-positive (+) UM (magnification, ×40). Inserts at ×360 magnification. (E) Schematic representation of metabolic shift in UM. The left panel shows the expression of ADP-positive lipid droplets (LDs) in tumours with normal nuclear expression of BAP1 (nBAP1+ UM). The right panel shows the expression of ADP-negative LDs with poor membrane stability in dissociation in nBAP1-negative tumours (nBAP1-UM). Two-tailed, unpaired *t*-test (****$p < 0.0001$).The schematics of Figure 2E were created with BioRender.com (license: HF24U9EYUB).

diffusely spread within the cytoplasm of nuclear BAP1-negative UM samples, suggesting potential lysis of the LD following increased levels of $CD163^+$ macrophages (Figure 2C,D). These findings suggest a relationship between loss of BAP1 expression and metabolic changes from normoxia toward lipid consumption during hypoxic conditions in high-risk UM, mainly featured by the decrease in available LDs containing adipophilin (Figure 2E).

Increased protein secretion reveals new metabolic prognostication signatures in pUM

To evaluate whether the metastatic risk of UM was associated with a decrease in lipid storage markers and an increase in lipid consumption (lipolysis) pathways in high-risk UM, we revisited the secretome profile of a local LOORG cohort of pUM samples ($n = 14$) previously cultured *ex vivo* [21]. The secretome included secreted proteins with a clinical score associated with hypoxia and lipid metabolism regulation (supplementary material, Tables S1 and S2). We observed that the higher the secretory activity (measured by the average of protein fold-change expression), the higher the metastatic risk score of these proteins, suggesting an increase in metabolic activity in high-risk UM (Figure 3A). Each secretome protein's risk distribution profile is associated with a clinical score, which ranges from −2 to 2, where −2 means no risk (blue) and +2 means high risk (red), shown in a heatmap sorted by the total expression level of individual proteins detected in the secretome. When proteins are sorted according to their expression levels, there is an evident shift from low- to high-risk clinical scores (Figure 3B). The corresponding gene symbols of these proteins were further uploaded into Xena browser to interrogate the transcript levels for these proteins in the GDC-TCGA-UM cohort, which was further sorted according to *BAP1* transcript levels. Surprisingly, the transcript profile for these proteins clustered into two main groups: upregulated genes following *BAP1* expression (predictors of good outcome) and upregulated genes following *BAP1* loss (predictors of poor outcome). Predictors of good outcomes are associated with survival (white), and predictors of poor outcomes are associated with death (black) (Figure 3C).

To validate the risk associated with the proteins identified in the secretome and identify those that could be part of a metabolic regulatory process in UM, we interrogated the impact on survival outcomes of these proteins in the GDC-TCGA-UM cohort ($n = 80$). All proteins and genes associated with poor outcomes in both cohorts were filtered for downstream analysis (supplementary material, Table S3). We performed a meta-analysis study on the functionality of these genes for their regulatory roles in the following metabolism subcategories: normoxia, hypoxia, lipid storage, and lipolysis. The category ranks were linked with the variance σ^2 of each gene expression within the GDC-TCGA-UM cohort to measure the plasticity of these genes (supplementary material, Table S2) and with the p value of Kaplan–Meier overall survival curves of each gene, to measure its impact on patient survival (supplementary material, Table S3). These variables were then uploaded in a network-category distribution cord plot, sorted primarily by survival impact (p value) and variance scores (σ^2, cord thickness) within each immune category. Genes that significantly impact the survival of UM patients with different statistical levels have cords coloured sky blue, orange, and red.

Interestingly, we observed that multigene predictors of good survival outcome in the cord plots clustered to categories of normoxia and lipid storage as one signature (Figure 3D, left), as opposed to multigene predictors of poor survival that clustered to categories of hypoxia and lipolysis, as a second signature (Figure 3D, right). The normoxia/lipid storage and hypoxia/lipolysis transcriptomic signatures were further evaluated between two UM cell lines with nBAP1 positive (Mel285) and negative (MP46) protein expression. We observed that some of the genes from both signatures produced the same differential expression profile of *BAP1* positive and *BAP1* negative UM samples from bulk RNA-seq data of the GDC-TCGA-UM cohort. For example, *SNTB2* appears upregulated in pUM tumours with *BAP1* loss as one of the poor outcome predictor signatures (Figure 3C,D). Still, *SNTB2* expression appears downregulated in the MP46 (nBAP1-negative) cell line compared with the Mel285 (nBAP1-positive) cell line (Figure 3E, right panel). Such differences might be explained by the fact that some of the identified signatures are differentially expressed by other cellular components of the TME rather than the tumour cells. Indeed, we observed that *SNTB2* and *FN1* genes were upregulated in co-cultures of the MP46 cell line with macrophages differentiated from monocytes of human peripheral blood (supplementary material, Figure S3A), suggesting that *BAP1* loss by tumour cells may trigger molecular processes that induce the expression of these signatures in stromal cells, such as TMAs. Therefore, 65.5% of upregulated normoxia/lipid storage signature can be represented by tumour cells, 34.4% can be represented by the TME in *BAP1*-positive tumours (Figure 3E, left doughnut plot), 33.3% of upregulated hypoxia/lipolysis signature can be represented by tumour cells, and the TME can represent 66.7% of the signature in *BAP1*-negative tumours (Figure 3E, right doughnut plot). Representative Kaplan–Meier survival curves for identified genes from both metabolic signatures are *SPP1* and *LAMA4* (good survival predictors) and *HTRA1* and *SNTB2* (poor survival predictors) (Figure 3F). These findings suggest that genes negatively correlated with *BAP1* and *PLIN2* levels in UM simultaneously associate with high protein metabolic index shifting from normoxia/lipid storage to hypoxia/lipolysis conditions.

Adipophilin-associated metabolic changes reveal novel therapeutic opportunities for UM

Discovering new adipophilin-based multigene metabolic signatures can establish the basis for developing

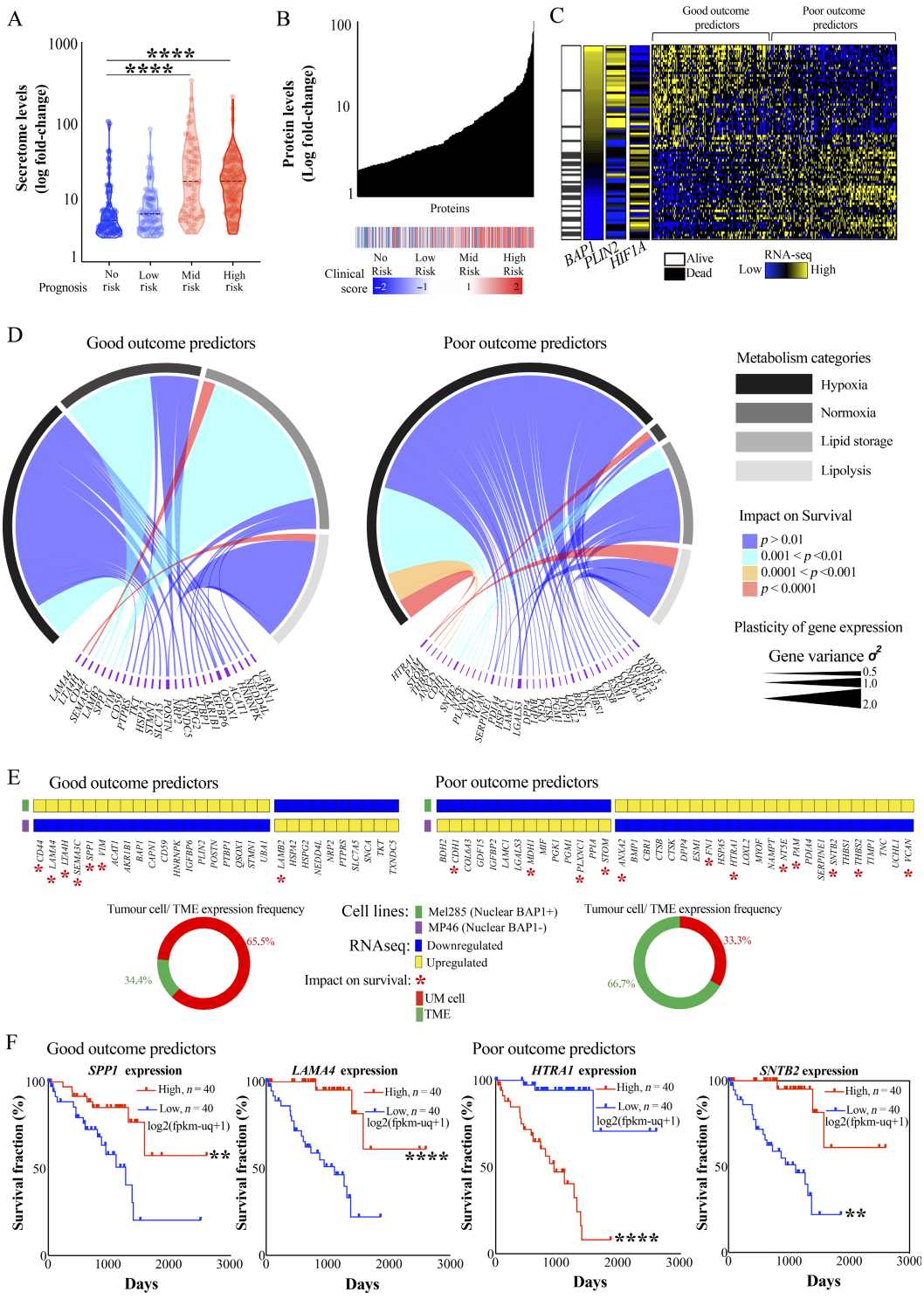

Figure 3. UM secretome reveals increased metabolic activity in high-risk UM patients and new hypoxia/lipid-storage prognostication signatures. (A) The secretome of 10 high-metastatic-risk and four low-metastatic-risk UM patients [21]. Patients were sorted into different risk groups, and violin plots show the average of protein fold-change expression in each risk group. (B) Risk distribution profile according to average expression level of each detected protein. Heatmap represents four different risk levels from no risk (blue) to high risk (red). (C) Clinical outcome profiles of *PLIN2*-correlated secretome genes in GDC-TCGA-UM cohort ($n = 80$). Genes from the UM secretome were uploaded in Xena browser and sorted according to *BAP1* gene expression levels. Two main clusters are upregulated genes (associated with survival, white) and upregulated genes that predict poor outcomes (associated with death, black). (D) Genes that significantly predicted good ($n = 26$) and poor ($n = 36$) GDC-TCGA-UM survival ($p < 0.05$) and that were previously described as regulators of hypoxia, normoxia, lipid storage, and lipolysis were clustered for survival and transcriptomic variance (σ^2). (E) Normalised TPM expression score (upregulated, yellow and downregulated, blue) of metabolic signatures obtained by next-generation sequencing RNA-seq of UM cells Mel285 (*BAP1*-positive, green) and MP46 (*BAP1*-negative, purple). Red stars highlight genes previously predicted to impact survival in both normoxia/lipid storage and hypoxia/lipolysis signatures. Doughnut plots represent the frequency of significant survival-impacting signatures consistently upregulated in UM cells (red) and predicted to be upregulated in the TME (red). (F) Survival profile of adipophilin-associated gene signatures. Kaplan–Meier survival curves from selected normoxia/lipid storage signatures (*SPP1* and *LAMA4*) and hypoxia/lipolysis signatures (*HTRA1* and *SNTB2*). The median of the mRNA gene expression determined the cutoff in the GDC-TCGA-UM cohort (****$p < 0.0001$; **$p < 0.01$).

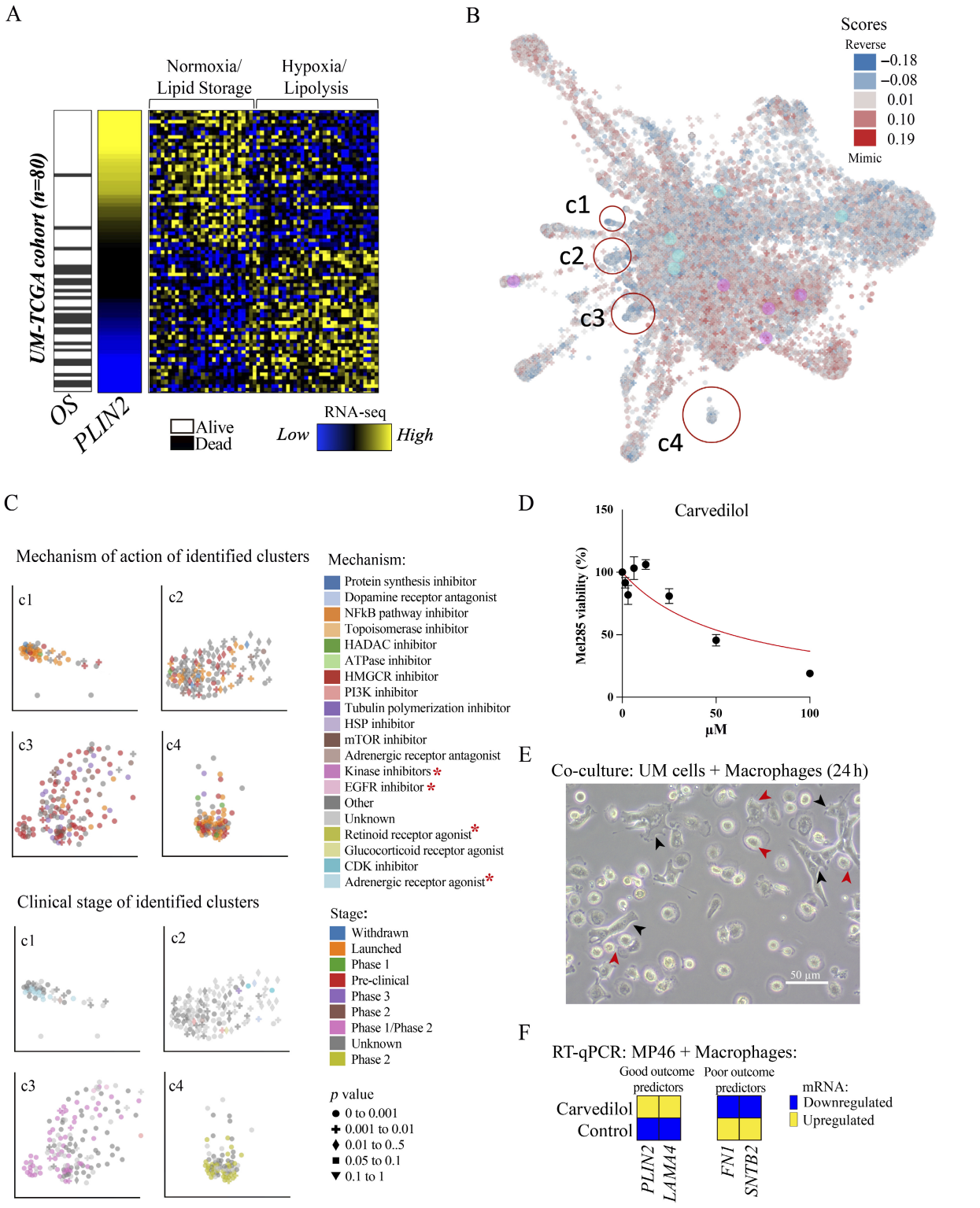

Figure 4. Identification of small molecules with the potential to reverse metabolic signature profile in UM. (A) Heatmap representation of mRNA expression levels of multigene signatures normoxia/lipid storage and hypoxia/lipolysis supervised by *PLIN2* in GDC-TCGA-UM cohort. Plots were generated using Xena browser. (B) L1000FWD drug-query plot from gene expression signatures against signatures created from human cell lines treated with over 20,000 small molecules and drugs. Scaffold L1000FWD plots depict different clusters, where red bubbles identify drugs with the potential to mimic the *PLIN2*-supervised multigene signature, and blue bubbles represent groups of drugs predicted to reverse the expression of these signatures. Clusters c1, c2, c3, and c4 represented the highest reverse score in the query. These clusters are predicted to upregulate normoxia/lipid storage signatures and downregulate hypoxia/lipolysis signatures in the GDC-TCGA-UM cohort. (C) The upper panel shows the distribution profile of clusters c1, c2, c3, and c4 and a list of the primary mechanism of action of the drugs that compose the four clusters. The lower panel shows the distribution profile of the clinical development stage of the drugs that compose the four clusters. (D) Viability curve of UM cell line Mel285 incubated with serial concentrations of carvedilol ranging from 0 to 100 µM for 24 h. The linear regression curve shows the cell viability in different concentrations relative to the untreated negative control (100%). (E) Representative image of a 2D co-culture of a UM cell line (black arrows) with human macrophages (red arrows). (F) Representative heatmaps of RT-qPCR results obtained from co-culture of MP46 cell line with human macrophages treated with 50 µM carvedilol for 24 h.

novel tailored therapeutic approaches for targeting metabolism in *BAP1*-deficient UM [19]. Identifying repurposed drugs with the potential to reverse UM metabolic evolution could be of great value for UM therapy. The differential expression metabolic signatures that significantly impact UM survival and have high expression variance in the GDC-TCGA-UM cohort are represented in the heatmap of Figure 4A. These signatures were uploaded into the L1000FWD web-based platform to predict small molecules with the ability to reverse hypoxia/lipolysis expression profile toward normoxia/lipid storage.

The drug signature profile is shown in a scaffold distribution plot, where red clusters represent groups of drugs tested in different human cells with the potential to mimic the multigene signature that drives the metabolic shift in UM. The blue clusters (c1, c2, c3, and c4) represent the group of drugs with the highest potential to mimic the metabolic transcriptome of BAP1-positive tumours or reverse the metabolic shift in BAP1-negative UM (Figure 4B). Interestingly, drugs observed in these clusters tend to have a similar mechanism of action, which is mainly represented by adrenergic receptor agonism (c1), Pi3K, CDK and tubulin inhibitors (c2), MEK and RAF inhibitors (c3), and retinoid receptor agonism (c4) and all identified drugs that are mainly launched or in Phase 2 or 3 of clinical development (Figure 4C). The top five drugs from each cluster, their mechanism of action, and their current clinical stage are presented in Table 2.

Since targeting metabolic pathways can be detrimental to cancer cell viability and survival [38], we evaluated the cytotoxic potential of nine predicted drugs from Table 3 against UM cells *in vitro*, including batimastat, bosutinib, carvedilol, palbociclib, fenbendazole, forskolin, selumetinib, tamibarotene, and vemurafenib. The viability curves are shown in supplementary material, Figure S3B, and the IC50 and non-linear fit (R^2) of viability curves for each drug is shown in Table 3. Interestingly, five out of nine tested drugs (55.5%) significantly impacted the viability of Mel285 cells, including bosutinib (IC50 = 8.8 μM), palbociclib (IC50 = 37.8 μM), carvedilol (IC50 = 58.1 μM), vemurafenib (IC50 = 200.3 μM), and forskolin (IC50 = 266.9 μM) (Table 3 and supplementary material, Figure S3B). Among the most effective drugs, carvedilol (Figure 4D) had intermediate cytostatic effects; it has been described as reversing HIF-1-induced hypoxia in heart failure models [39].

Therefore, we evaluated whether subdoses of carvedilol could reverse the expression of poor-outcome-predicting signatures or mimic/enhance the expression of good-outcome-predicting signatures in co-cultures of the BAP1-negative MP46 cell line with human macrophages obtained from peripheral blood. A representative picture of UM cells co-cultured with human macrophages is shown in Figure 4E. As predicted, carvedilol restored *PLIN2* levels, upregulated *LAMA4* (normoxia/lipid storage signatures), and downregulated *FN1* and *SNBT2* (hypoxia/lipolysis signatures) (Figure 4F and supplementary material, Figure S3C). These findings suggest that the predicted drugs have the potential to impact UM cell viability, restore the expression of *PLIN2* in BAP1-negative tumours, and reverse the expression of metabolic signatures associated with poor survival outcomes.

DISCUSSION

Adipophilin has emerged as a prognostic biomarker in different cancer types, including colorectal, lung, breast, ovarian, clear cell renal cell carcinoma, and cutaneous malignant melanoma [40–45]. UM prognostication for predicting metastatic risk and patient management, involves the combination of clinical, morphological,

Table 2. Description of L1000FWD-identified drugs that reverse the metabolic shift in BAP1 tumours.

Cluster	Drug name	Mechanism of action	Clinical stage	Reference	Clinical trial identifier
c1	Procaterol	Adrenergic receptor agonist	Launched	[69]	NCT02885636
	Forskolin	Adenyl cyclase activator	Launched	[70]	NCT00864578
	Formoterol	Adrenergic receptor agonist	Launched	[71]	NCT02796651
	Isoxsuprine	Adrenergic receptor agonist	Launched	[72]	NCT03752307
	Orciprenaline	Adrenergic receptor agonist	Launched	[73]	N/A
c2	BRD-K81647657	Pi3K inhibitor	Preclinical	[74]	N/A
	Carvedilol	Adrenergic receptor agonist	Launched	[67]	NCT00924833
	Fludroxycortide	Glucocorticoid receptor agonist	Launched	[75]	NCT01996930
	Fenbendazole	Tubulin polymerisation inhibitor	Launched	[76]	NCT04713787
	Palbociclib	CDK inhibitor	Launched	[77]	NCT02334527
c3	PD-184352	MEK inhibitor	Phase 2	[78]	N/A
	PD-0325901	MEK inhibitor	Phase 2	[79]	NCT02096471
	Selumetinib	MEK inhibitor	Phase 3	[80]	NCT01933932
	Vemurafenib	RAF inhibitor	Launched	[81]	NCT01585415
	Bosutinib	Abl Kinase inhibitor	Launched	[82]	NCT04793399
c4	Tamibarotene	Retinoid receptor agonist	Launched	[83]	NCT02807558
	Tretinoin	Retinoid receptor agonist	Launched	[84]	NCT02807558
	Batimastat	HDAC inhibitor	Phase 3	[85]	N/A
	GW-501516	Cyclooxygenase inhibitor	Phase 2	[86]	N/A
	AM-580	Retinoid receptor agonist	Preclinical	[87]	N/A

HDAC, histone deacetylases.

Table 3. IC50 and R^2 scores from non-linear dose response regression analysis of UM cells treated with predictive drugs for 24 h.

Drug name	Mel285	
	IC50 (μM)	R^2
Bosutinib	8.8	0.806
Palbociclib	37.8	0.723
Carvedilol	58.1	0.668
Vemurafenib	200.3	0.718
Forskolin	266.9	0.390
Batimastat	>500	0.000
Fenbendazole	>500	0.000
Selumetinib	>500	0.000
Tamibarotene	>500	0.000

and genetic analyses [46,47]. Current genetic prognostic markers and biochemical pathways correlated to UM metastasis were recently reviewed [48]. In this study, we underscored the prognostic potential of adipophilin in UM for the first time, uncovering a network of adipophilin-dependent metabolic changes associated with *BAP1* loss and clinical outcomes. Understanding UM-specific immunosuppression driven by *BAP1* loss has been advanced by nCounter transcriptome sequencing of primary and metastatic UM samples [3]. Changes in BAP1 expression have recently been linked to significant effects on energy metabolism in UM [11–13]. Our findings provide insights into the role of adipophilin in lipid storage and lipid metabolism, where adipophilin levels are lost in the context of oxygen deprivation during hypoxia, promoting a metabolic immunosuppressive TME that favours UM progression and increased metastatic risk. When binding to LDs, adipophilin is stabilised and functions as a gatekeeper of LD, attenuating lipolytic metabolism [16,49–51]. However, competition between adipophilin and other proteins of the PAT (perilipin, ADRP, TIP47) family leads to rapid degradation of adipophilin in LDs. Indeed, M2-like macrophages are associated with immunosuppression and tumour progression in UM with BAP1 loss [3,22]. Our co-culture approach using UM cell lines with human macrophages supports this relationship, where the expression of poor-outcome predictor signature *SNTB2* increases in the context of BAP1 loss. Increased levels of $CD163^+$ TAMs in the context of reduced adipophilin-positive LD may be associated with lipid catabolism favouring M2 polarisation and proliferation. As specialised phagocytic cells, M2 macrophages uptake lipids from both engulfed dying cells or LD in the TME, which are then processed by acid lipases within the lysosomes, leading to the generation of free FA that is subsequently transported into mitochondria for ATP generation under hypoxia conditions, reviewed in [52]. Also, insufficient oxygenation in the 'inflamed' TME induces the upregulation of HIF-1 [53], reprogramming TME metabolism into oxygen-independent mechanisms for energy generation such as *de novo* lipogenesis [54–56]. High levels of FA during hypoxia, in combination with *PLIN2* downregulation, lead to liver lipotoxicity [57,58]. Indeed, the inability to store FA in LDs also leads to CD8+ T-cell exhaustion [59], while Tregs enhance their FA uptake and become resistant to lipotoxicity [60,61]. We propose that low levels of *PLIN2* under hypoxia conditions are involved in impaired lipolysis control. Consequently, TAMs within the UM TME acquire a pro-tumorigenic phenotype facilitating immune suppression and, eventually, immunotherapy resistance.

The regulatory role of BAP1 in lipid metabolism has also been reported in preclinical models [12]. Liver-specific deletion of *BAP1* led to reduced levels of specific genes that included *PLIN2* and resulted in lipid mismanagement, liver inflammation, and fibrosis [12,62]. Accordingly, our data suggest that adipophilin loss in BAP1-negative UM, which is also associated with poor outcomes, may be one of the contributing factors in making the liver a preferable metastatic site of UM cells.

Metabolic alterations in high-risk UM may be a suitable therapeutic opportunity for this devastating disease, which is universally refractory to immunotherapies [63]. Dissecting the molecular process and network links in metabolic heterogenous UM may provide tailored therapeutic approaches for *BAP1*-deficient UM [19]. In our drug-discovery screening approach using current identified metabolic UM signatures to query the L1000FWD application [33], we identified specific clusters of drugs predominantly homogenous in terms of their potential to reverse the hypoxia/lipolysis signature profile to normoxia/lipid storage profile in *BAP1* negative UM. The main category of drugs includes adrenergic, retinoid, and glucocorticoid receptor agonists, HDAC, Pi3K, MEK, and RAF inhibitors.

Surprisingly, some of these drugs have already been tested in UM melanoma clinical trials, including HDAC inhibitors (NCT02068586, NCT03022565) [64,65], selumetinib, which impacted progression-free survival and response rate but not overall survival in UM [66], and in UM preclinical research, including carvedilol, which was recently described as eliciting anti-tumour responses in UM 3D spheroids [67], and vemurafenib, which induces autophagic cell death in UM cells with V600E *in vitro* [68].

The cytotoxic potential of five identified drugs was validated in UM cell lines. Bosutinib, a BCR–ABL small molecule inhibitor used for treating chronic myelogenous leukaemia, showed the strongest cytotoxic effect, and carvedilol, an adrenergic receptor antagonist, effectively modulated identified prognostication signatures. Importantly, BCR–ABL has been described as reducing the stability of BAP1 in chronic myeloid leukaemia [39], and the relationship of BCR–ABL with BAP1 in UM remains to be elucidated.

In conclusion, a decrease in adipophilin levels in high-risk UM is associated with a transitional state of normoxia and lipid storage to hypoxia and lipolysis in the TME of pUM. Such features may play a key role in BAP1-induced immunosuppression and metastasis development. Our findings uncover new grounds for developing therapeutic strategies for UM in view of its metabolic evolution associated with *BAP1* loss and

clinical outcomes. New metabolic UM signatures associated with adipophilin might identify UM patients that could benefit from tailored metabolic targeted therapies that could now be developed in preclinical studies.

Acknowledgements

This study was funded by grants from the Academy of Finland (to CRF), Jane and Aatos Erkko Foundation (to CRF), Sigrid Jusélius Foundation (to CRF), InFlames Flagship (to CRF), Turku Doctoral Programme of Molecular Medicine (to EM), and the Northwest Cancer Research Fund (to SEC). This project also received funding from the European Union's Horizon 2020 research UM-Cure. We thank the Institute of Systems, Molecular and Integrative Biology at the University of Liverpool for supporting the metabolomics studies. We thank Karen Aughton for her support with culture advice using UM cell lines. Immunohistochemistry staining was performed by the Liverpool Clinical Laboratories at the Liverpool University Hospitals Foundation Trust, Liverpool, UK. We thank Dr Sophie Thornton for conducting multiplex ligation-dependent probe amplification (MLPA) analysis. We thank the Finnish Functional Genomics Centre, supported by the University of Turku, Åbo Akademi University, and Biocenter Finland for supporting RNA-seq data studies.

Author contributions statement

MM, EM, SEC and CRF contributed to the conceptualisation of the study. MM, EM, SAK, AM, HK, SEC and CRF contributed to data curation, formal study analysis, study investigation, data visualisation, methodology validation, and wrote the manuscript. EM performed the research, and performed meta-analysis of literature metabolomics. SAK performed *in vitro* cytotoxicity studies. AM performed computational analysis of transcriptomic datasets, and developed computing methodologies. HK: enabled access to biobank resources and supported with funding acquisition. SEC undertook student supervision, funding acquisition, administration of local project and funding, and contributed to manuscript revision and editing. CRF conducted formal analysis of the entire study, supervised the students and research, contributed to funding acquisition, data validation, revised data visualisation, methodology development, wrote the original draft, performed the revision and editing and administred the project.

Data availability statement

Primary UM transcriptomic RNA-seq data are available at the GDC portal (https://portal.gdc.cancer.gov), and normalised cases can be downloaded from the UCSC Xena platform (https://xenabrowser.net/). The normal retina transcriptome cohort is available for download at (https://eyeintegration.nei.nih.gov), in which *PLIN2* gene code ENST00000276914.6 was used for gene expression visualisation of the Gene 2019 dataset. RNA-seq data from UM cell lines have been deposited in GEO, Accession No. GSE225347 (https://www.ncbi.nlm.nih.gov/geo/query/acc.cgi?acc=GSE225347).

References

1. Yang J, Manson DK, Marr BP, *et al*. Treatment of uveal melanoma: where are we now? *Ther Adv Med Oncol* 2018; **10:** 1758834018757175.
2. Heppt MV, Heinzerling L, Kähler KC, *et al*. Prognostic factors and outcomes in metastatic uveal melanoma treated with programmed cell death-1 or combined PD-1/cytotoxic T-lymphocyte antigen-4 inhibition. *Eur J Cancer* 2017; **82:** 56–65.
3. Figueiredo CR, Kalirai H, Sacco JJ, *et al*. Loss of BAP1 expression is associated with an immunosuppressive microenvironment in uveal melanoma, with implications for immunotherapy development. *J Pathol* 2020; **250:** 420–439.
4. Farquhar N, Thornton S, Coupland SE, *et al*. Patterns of BAP1 protein expression provide insights into prognostic significance and the biology of uveal melanoma. *J Pathol Clin Res* 2018; **4:** 26–38.
5. Ma RY, Black A, Qian BZ. Macrophage diversity in cancer revisited in the era of single-cell omics. *Trends Immunol* 2022; **43:** 546–563.
6. Wu SZ, Al-Eryani G, Roden DL, *et al*. A single-cell and spatially resolved atlas of human breast cancers. *Nat Genet* 2021; **53:** 1334–1347.
7. Han A, Purwin TJ, Aplin AE. Roles of the BAP1 Tumor Suppressor in Cell Metabolism. *Cancer Res* 2021; **81:** 2807–2814.
8. Carbone M, Harbour JW, Brugarolas J, *et al*. Biological mechanisms and clinical significance of *BAP1* mutations in human cancer. *Cancer Discov* 2020; **10:** 1103–1120.
9. Yang LV. Tumor microenvironment and metabolism. *Int J Mol Sci* 2017; **18:** 2729.
10. Phan LM, Yeung S-CJ, Lee M-H. Cancer metabolic reprogramming: importance, main features, and potentials for precise targeted anticancer therapies. *Cancer Biol Med* 2014; **11:** 1–19.
11. Hebert L, Bellanger D, Guillas C, *et al*. Modulating BAP1 expression affects ROS homeostasis, cell motility and mitochondrial function. *Oncotarget* 2017; **8:** 72513–72527.
12. Baughman JM, Rose CM, Kolumam G, *et al*. NeuCode proteomics reveals Bap1 regulation of metabolism. *Cell Rep* 2016; **16:** 583–595.
13. Fiorentzis M, Kalirai H, Katopodis P, *et al*. Adipophilin expression in primary and metastatic uveal melanoma: a pilot study. *Graefes Arch Clin Exp Ophthalmol* 2017; **255:** 1049–1051.
14. Bickel PE, Tansey JT, Welte MA. PAT proteins, an ancient family of lipid droplet proteins that regulate cellular lipid stores. *Biochim Biophys Acta* 2009; **1791:** 419–440.
15. Straub BK, Herpel E, Singer S, *et al*. Lipid droplet-associated PAT-proteins show frequent and differential expression in neoplastic steatogenesis. *Mod Pathol* 2010; **23:** 480–492.
16. Sztalryd C, Brasaemle DL. The perilipin family of lipid droplet proteins: gatekeepers of intracellular lipolysis. *Biochim Biophys Acta Mol Cell Biol Lipids* 2017; **1862:** 1221–1232.
17. Hickenbottom SJ, Kimmel AR, Londos C, *et al*. Structure of a lipid droplet protein; the PAT family member TIP47. *Structure* 2004; **12:** 1199–1207.
18. Conte M, Franceschi C, Sandri M, *et al*. Perilipin 2 and age-related metabolic diseases: a new perspective. *Trends Endocrinol Metab* 2016; **27:** 893–903.
19. Han A, Purwin TJ, Bechtel N, *et al*. BAP1 mutant uveal melanoma is stratified by metabolic phenotypes with distinct vulnerability to metabolic inhibitors. *Oncogene* 2021; **40:** 618–632.

20. Robertson AG, Shih J, Yau C, *et al*. Integrative analysis identifies four molecular and clinical subsets in uveal melanoma. *Cancer Cell* 2017; **32:** 204–220.e215.
21. Angi M, Kalirai H, Prendergast S, *et al*. In-depth proteomic profiling of the uveal melanoma secretome. *Oncotarget* 2016; **7:** 49623–49635.
22. Krishna Y, Acha-Sagredo A, Sabat-Pośpiech D, *et al*. Transcriptome profiling reveals new insights into the immune microenvironment and upregulation of novel biomarkers in metastatic uveal melanoma. *Cancers (Basel)* 2020; **12:** 2832.
23. Ireland L, Santos A, Campbell F, *et al*. Blockade of insulin-like growth factors increases efficacy of paclitaxel in metastatic breast cancer. *Oncogene* 2018; **37:** 2022–2036.
24. Borriello L, Coste A, Traub B, *et al*. Primary tumor associated macrophages activate programs of invasion and dormancy in disseminating tumor cells. *Nat Commun* 2022; **13:** 626.
25. Figueiredo CR, Azevedo RA, Mousdell S, *et al*. Blockade of MIF-CD74 signalling on macrophages and dendritic cells restores the antitumour immune response against metastatic melanoma. *Front Immunol* 2018; **9:** 1132.
26. Bray NL, Pimentel H, Melsted P, *et al*. Near-optimal probabilistic RNA-seq quantification. *Nat Biotechnol* 2016; **34:** 525–527.
27. Krishna Y, McCarthy C, Kalirai H, *et al*. Inflammatory cell infiltrates in advanced metastatic uveal melanoma. *Hum Pathol* 2017; **66:** 159–166.
28. Angi M, Kalirai H, Taktak A, *et al*. Prognostic biopsy of choroidal melanoma: an optimised surgical and laboratory approach. *Br J Ophthalmol* 2017; **101:** 1143–1146.
29. Nosavanh L, Yu D-H, Jaehnig EJ, *et al*. Cell-autonomous activation of Hedgehog signaling inhibits brown adipose tissue development. *Proc Natl Acad Sci U S A* 2015; **112:** 5069–5074.
30. Goodwin J, Neugent ML, Lee SY, *et al*. The distinct metabolic phenotype of lung squamous cell carcinoma defines selective vulnerability to glycolytic inhibition. *Nat Commun* 2017; **8:** 15503.
31. Ross MH, Esser AK, Fox GC, *et al*. Bone-induced expression of integrin β3 enables targeted nanotherapy of breast cancer metastases. *Cancer Res* 2017; **77:** 6299–6312.
32. Gu Z, Gu L, Eils R, *et al*. circlize Implements and enhances circular visualization in R. *Bioinformatics* 2014; **30:** 2811–2812.
33. Wang Z, Lachmann A, Keenan AB, *et al*. L1000FWD: fireworks visualization of drug-induced transcriptomic signatures. *Bioinformatics* 2018; **34:** 2150–2152.
34. Swamy V, McGaughey D. Eye in a disk: eyeIntegration Human Pan-Eye and Body Transcriptome Database Version 1.0. *Invest Ophthalmol Vis Sci* 2019; **60:** 3236–3246.
35. Chatsirisupachai K, Lesluyes T, Paraoan L, *et al*. An integrative analysis of the age-associated multi-omic landscape across cancers. *Nat Commun* 2021; **12:** 2345.
36. Li S, Yu J, Huber A, *et al*. Metabolism drives macrophage heterogeneity in the tumor microenvironment. *Cell Rep* 2022; **39:** 110609.
37. Munir R, Lisec J, Swinnen JV, *et al*. Lipid metabolism in cancer cells under metabolic stress. *Br J Cancer* 2019; **120:** 1090–1098.
38. Ackerman D, Simon MC. Hypoxia, lipids, and cancer: surviving the harsh tumor microenvironment. *Trends Cell Biol* 2014; **24:** 472–478.
39. Shyu KG, Lu MJ, Chang H, *et al*. Carvedilol modulates the expression of hypoxia-inducible factor-1alpha and vascular endothelial growth factor in a rat model of volume-overload heart failure. *J Card Fail* 2005; **11:** 152–159.
40. Tolkach Y, Lüders C, Meller S, *et al*. Adipophilin as prognostic biomarker in clear cell renal cell carcinoma. *Oncotarget* 2017; **8:** 28672–28682.
41. Yoshikawa K, Ishida M, Yanai H, *et al*. Adipophilin expression is an independent marker for poor prognosis of patients with triple-negative breast cancer: an immunohistochemical study. *PLoS One* 2020; **15:** e0242563.
42. Shin SA, Na HY, Choe JY, *et al*. The expression of adipophilin is frequently found in solid subtype adenocarcinoma and is associated with adverse outcomes in lung adenocarcinoma. *J Pathol Transl Med* 2018; **52:** 357–362.
43. Matsubara J, Honda K, Ono M, *et al*. Identification of adipophilin as a potential plasma biomarker for colorectal cancer using label-free quantitative mass spectrometry and protein microarray. *Cancer Epidemiol Biomarkers Prev* 2011; **20:** 2195–2203.
44. Fujimoto M, Matsuzaki I, Nishitsuji K, *et al*. Adipophilin expression in cutaneous malignant melanoma is associated with high proliferation and poor clinical prognosis. *Lab Invest* 2020; **100:** 727–737.
45. Iwahashi N, Ikezaki M, Fujimoto M, *et al*. Lipid droplet accumulation independently predicts poor clinical prognosis in high-grade serous ovarian carcinoma. *Cancers (Basel)* 2021; **13:** 5251.
46. Damato B, Eleuteri A, Taktak AF, *et al*. Estimating prognosis for survival after treatment of choroidal melanoma. *Prog Retin Eye Res* 2011; **30:** 285–295.
47. Eleuteri A, Taktak AFG, Coupland SE, *et al*. Prognostication of metastatic death in uveal melanoma patients: a Markov multi-state model. *Comput Biol Med* 2018; **102:** 151–156.
48. Gallenga CE, Franco E, Adamo GG, *et al*. Genetic basis and molecular mechanisms of uveal melanoma metastasis: a focus on prognosis. *Front Oncol* 2022; **12:** 828112.
49. Bell M, Wang H, Chen H, *et al*. Consequences of lipid droplet coat protein downregulation in liver cells: abnormal lipid droplet metabolism and induction of insulin resistance. *Diabetes* 2008; **57:** 2037–2045.
50. Listenberger LL, Ostermeyer-Fay AG, Goldberg EB, *et al*. Adipocyte differentiation-related protein reduces the lipid droplet association of adipose triglyceride lipase and slows triacylglycerol turnover. *J Lipid Res* 2007; **48:** 2751–2761.
51. Brasaemle DL, Barber T, Wolins NE, *et al*. Adipose differentiation-related protein is an ubiquitously expressed lipid storage droplet-associated protein. *J Lipid Res* 1997; **38:** 2249–2263.
52. Viola A, Munari F, Sánchez-Rodríguez R, *et al*. The metabolic signature of macrophage responses. *Front Immunol* 2019; **10:** 1462.
53. Rius J, Guma M, Schachtrup C, *et al*. NF-kappaB links innate immunity to the hypoxic response through transcriptional regulation of HIF-1alpha. *Nature* 2008; **453:** 807–811.
54. Eales KL, Hollinshead KE, Tennant DA. Hypoxia and metabolic adaptation of cancer cells. *Oncogenesis* 2016; **5:** e190.
55. Baenke F, Peck B, Miess H, *et al*. Hooked on fat: the role of lipid synthesis in cancer metabolism and tumour development. *Dis Model Mech* 2013; **6:** 1353–1363.
56. Schug ZT, Peck B, Jones DT, *et al*. Acetyl-CoA synthetase 2 promotes acetate utilization and maintains cancer cell growth under metabolic stress. *Cancer Cell* 2015; **27:** 57–71.
57. Tsai TH, Chen E, Li L, *et al*. The constitutive lipid droplet protein PLIN2 regulates autophagy in liver. *Autophagy* 2017; **13:** 1130–1144.
58. Imai Y, Boyle S, Varela GM, *et al*. Effects of perilipin 2 antisense oligonucleotide treatment on hepatic lipid metabolism and gene expression. *Physiol Genomics* 2012; **44:** 1125–1131.
59. Manzo T, Prentice BM, Anderson KG, *et al*. Accumulation of long-chain fatty acids in the tumor microenvironment drives dysfunction in intrapancreatic CD8+ T cells. *J Exp Med* 2020; **217:** e20191920.
60. Wang H, Franco F, Tsui YC, *et al*. CD36-mediated metabolic adaptation supports regulatory T cell survival and function in tumors. *Nat Immunol* 2020; **21:** 298–308.
61. Pacella I, Procaccini C, Focaccetti C, *et al*. Fatty acid metabolism complements glycolysis in the selective regulatory T cell expansion during tumor growth. *Proc Natl Acad Sci U S A* 2018; **115:** E6546–e6555.
62. Najt CP, Senthivinayagam S, Aljazi MB, *et al*. Liver-specific loss of Perilipin 2 alleviates diet-induced hepatic steatosis, inflammation,

and fibrosis. *Am J Physiol Gastrointest Liver Physiol* 2016; **310:** G726–G738.
63. Sacco JJ, Kalirai H, Kenyani J, *et al*. Recent breakthroughs in metastatic uveal melanoma: a cause for optimism? *Future Oncol* 2018; **14:** 1335–1338.
64. Faião-Flores F, Smalley KS. Histone deacetylase inhibitors: a promising partner for MEK inhibitors in uveal melanoma? *Melanoma Manag* 2019; **6:** MMT29.
65. Landreville S, Agapova OA, Matatall KA, *et al*. Histone deacetylase inhibitors induce growth arrest and differentiation in uveal melanoma. *Clin Cancer Res* 2012; **18:** 408–416.
66. Carvajal RD, Sosman JA, Quevedo JF, *et al*. Effect of selumetinib vs chemotherapy on progression-free survival in uveal melanoma: a randomized clinical trial. *JAMA* 2014; **311:** 2397–2405.
67. Farhoumand LS, Fiorentzis M, Kraemer MM, *et al*. The adrenergic receptor antagonist carvedilol elicits anti-tumor responses in uveal melanoma 3D tumor spheroids and may serve as co-adjuvant therapy with radiation. *Cancers (Basel)* 2022; **14:** 3097.
68. Zhao Y, Wang W, Min I, *et al*. BRAF V600E-dependent role of autophagy in uveal melanoma. *J Cancer Res Clin Oncol* 2017; **143:** 447–455.
69. Tashimo H, Yamashita N, Ishida H, *et al*. Effect of procaterol, a beta(2) selective adrenergic receptor agonist, on airway inflammation and hyperresponsiveness. *Allergol Int* 2007; **56:** 241–247.
70. Qi C, Lavriha P, Mehta V, *et al*. Structural basis of adenylyl cyclase 9 activation. *Nat Commun* 2022; **13:** 1045.
71. Becker AB, Simons FE. Formoterol, a new long-acting selective beta 2-adrenergic receptor agonist: double-blind comparison with salbutamol and placebo in children with asthma. *J Allergy Clin Immunol* 1989; **84:** 891–895.
72. Marzo A, Zava D, Coa K, *et al*. Pharmacokinetics of isoxsuprine hydrochloride administered orally and intramuscularly to female healthy volunteers. *Arzneimittelforschung* 2009; **59:** 455–460.
73. Khammy MM, Truong CKH, Wright CE, *et al*. The β(2)-adrenoceptor agonist bronchodilators terbutaline and orciprenaline are also weak α(1)-adrenoceptor antagonists. *Eur J Pharmacol* 2020; **882:** 173304.
74. Chicote J, Yuste VJ, Boix J, *et al*. Cell death triggered by the autophagy inhibitory drug 3-methyladenine in growing conditions proceeds With DNA damage. *Front Pharmacol* 2020; **11:** 580343.
75. Wang AL, Panganiban R, Qiu W, *et al*. Drug repurposing to treat glucocorticoid resistance in asthma. *J Pers Med* 2021; **11:** 175.
76. Spagnuolo PA, Hu J, Hurren R, *et al*. The antihelmintic flubendazole inhibits microtubule function through a mechanism distinct from Vinca alkaloids and displays preclinical activity in leukemia and myeloma. *Blood* 2010; **115:** 4824–4833.
77. Abdelmalak M, Singh R, Anwer M, *et al*. The renaissance of CDK inhibitors in breast cancer therapy: an update on clinical trials and therapy resistance. *Cancers (Basel)* 2022; **14:** 5388.
78. Allen LF, Sebolt-Leopold J, Meyer MB. CI-1040 (PD184352), a targeted signal transduction inhibitor of MEK (MAPKK). *Semin Oncol* 2003; **30:** 105–116.
79. Haura EB, Ricart AD, Larson TG, *et al*. A phase II study of PD-0325901, an oral MEK inhibitor, in previously treated patients with advanced non-small cell lung cancer. *Clin Cancer Res* 2010; **16:** 2450–2457.
80. Jänne PA, van den Heuvel MM, Barlesi F, *et al*. Selumetinib plus docetaxel compared with docetaxel alone and progression-free survival in patients with KRAS-mutant advanced non-small cell lung cancer: the SELECT-1 randomized clinical trial. *JAMA* 2017; **317:** 1844–1853.
81. Kaley T, Touat M, Subbiah V, *et al*. BRAF inhibition in BRAF(V600)-mutant gliomas: results from the VE-BASKET study. *J Clin Oncol* 2018; **36:** 3477–3484.
82. Brümmendorf TH, Cortes JE, Milojkovic D, *et al*. Bosutinib versus imatinib for newly diagnosed chronic phase chronic myeloid leukemia: final results from the BFORE trial. *Leukemia* 2022; **36:** 1825–1833.
83. Takeshita A, Asou N, Atsuta Y, *et al*. Tamibarotene maintenance improved relapse-free survival of acute promyelocytic leukemia: a final result of prospective, randomized, JALSG-APL204 study. *Leukemia* 2019; **33:** 358–370.
84. Shimono K, Tung WE, Macolino C, *et al*. Potent inhibition of heterotopic ossification by nuclear retinoic acid receptor-γ agonists. *Nat Med* 2011; **17:** 454–460.
85. Parsons SL, Watson SA, Steele RJ. Phase I/II trial of batimastat, a matrix metalloproteinase inhibitor, in patients with malignant ascites. *Eur J Surg Oncol* 1997; **23:** 526–531.
86. Coll T, Alvarez-Guardia D, Barroso E, *et al*. Activation of peroxisome proliferator-activated receptor-{delta} by GW501516 prevents fatty acid-induced nuclear factor-{kappa}B activation and insulin resistance in skeletal muscle cells. *Endocrinology* 2010; **151:** 1560–1569.
87. Drowley L, McPheat J, Nordqvist A, *et al*. Discovery of retinoic acid receptor agonists as proliferators of cardiac progenitor cells through a phenotypic screening approach. *Stem Cells Transl Med* 2020; **9:** 47–60.
88. Xiaofei C, Yanqing L, Dongkai Z, *et al*. Identification of cathepsin B as a novel target of hypoxia-inducible factor-1-alpha in HepG2 cells. *Biochem Biophys Res Commun* 2018; **503:** 1057–1062.
89. Mizunoe Y, Kobayashi M, Hoshino S, *et al*. Cathepsin B overexpression induces degradation of perilipin 1 to cause lipid metabolism dysfunction in adipocytes. *Sci Rep* 2020; **10:** 634.
90. Thibeaux S, Siddiqi S, Zhelyabovska O, *et al*. Cathepsin B regulates hepatic lipid metabolism by cleaving liver fatty acid-binding protein. *J Biol Chem* 2018; **293:** 1910–1923.
91. Matarrese P, Ascione B, Ciarlo L, *et al*. Cathepsin B inhibition interferes with metastatic potential of human melanoma: an in vitro and in vivo study. *Mol Cancer* 2010; **9:** 207.
92. Ma Q, Yu M, Zhou B, *et al*. QSOX1 promotes mitochondrial apoptosis of hepatocellular carcinoma cells during anchorage-independent growth by inhibiting lipid synthesis. *Biochem Biophys Res Commun* 2020; **532:** 258–264.
93. Shi CY, Fan Y, Liu B, *et al*. HIF1 contributes to hypoxia-induced pancreatic cancer cells invasion via promoting QSOX1 expression. *Cell Physiol Biochem* 2013; **32:** 561–568.
94. Supanji SM, Hasan MZ, *et al*. HtrA1 is induced by oxidative stress and enhances cell senescence through p38 MAPK pathway. *Exp Eye Res* 2013; **112:** 79–92.
95. Klose R, Adam MG, Weis EM, *et al*. Inactivation of the serine protease HTRA1 inhibits tumor growth by deregulating angiogenesis. *Oncogene* 2018; **37:** 4260–4272.
96. Wang N, Eckert KA, Zomorrodi AR, *et al*. Down-regulation of HtrA1 activates the epithelial-mesenchymal transition and ATM DNA damage response pathways. *PLoS One* 2012; **7:** e39446.
97. Tiaden AN, Bahrenberg G, Mirsaidi A, *et al*. Novel function of serine protease HTRA1 in inhibiting adipogenic differentiation of human mesenchymal stem cells via MAP kinase-mediated MMP upregulation. *Stem Cells* 2016; **34:** 1601–1614.
98. Baldi A, De Luca A, Morini M, *et al*. The HtrA1 serine protease is down-regulated during human melanoma progression and represses growth of metastatic melanoma cells. *Oncogene* 2002; **21:** 6684–6688.
99. Soto-Pantoja DR, Sipes JM, Martin-Manso G, *et al*. Dietary fat overcomes the protective activity of thrombospondin-1 signaling in the Apc(Min/+) model of colon cancer. *Oncogenesis* 2016; **5:** e230.
100. Gutierrez LS, Gutierrez J. Thrombospondin 1 in metabolic diseases. *Front Endocrinol (Lausanne)* 2021; **12:** 638536.

101. Jayachandran A, Anaka M, Prithviraj P, *et al*. Thrombospondin 1 promotes an aggressive phenotype through epithelial-to-mesenchymal transition in human melanoma. *Oncotarget* 2014; **5:** 5782–5797.
102. Alvarez Secord A, Bernardini MQ, Broadwater G, *et al*. TP53 status is associated with thrombospondin1 expression in vitro. *Front Oncol* 2013; **3:** 269.
103. Graja A, Garcia-Carrizo F, Jank AM, *et al*. Loss of periostin occurs in aging adipose tissue of mice and its genetic ablation impairs adipose tissue lipid metabolism. *Aging Cell* 2018; **17:** e12810.
104. González-González L, Alonso J. Periostin: a matricellular protein with multiple functions in cancer development and progression. *Front Oncol* 2018; **8:** 225.
105. Baril P, Gangeswaran R, Mahon PC, *et al*. Periostin promotes invasiveness and resistance of pancreatic cancer cells to hypoxia-induced cell death: role of the beta4 integrin and the PI3k pathway. *Oncogene* 2007; **26:** 2082–2094.
106. Guo X, Xue H, Shao Q, *et al*. Hypoxia promotes glioma-associated macrophage infiltration via periostin and subsequent M2 polarization by upregulating TGF-beta and M-CSFR. *Oncotarget* 2016; **7:** 80521–80542.
107. Kotobuki Y, Yang L, Serada S, *et al*. Periostin accelerates human malignant melanoma progression by modifying the melanoma microenvironment. *Pigment Cell Melanoma Res* 2014; **27:** 630–639.
108. Levine JA, Oleaga C, Eren M, *et al*. Role of PAI-1 in hepatic steatosis and dyslipidemia. *Sci Rep* 2021; **11:** 430.
109. Rofstad EK, Rasmussen H, Galappathi K, *et al*. Hypoxia promotes lymph node metastasis in human melanoma xenografts by upregulating the urokinase-type plasminogen activator receptor. *Cancer Res* 2002; **62:** 1847–1853.
110. Liao H, Hyman MC, Lawrence DA, *et al*. Molecular regulation of the PAI-1 gene by hypoxia: contributions of Egr-1, HIF-1alpha, and C/EBPalpha. *FASEB J* 2007; **21:** 935–949.
111. Blomme A, Costanza B, de Tullio P, *et al*. Myoferlin regulates cellular lipid metabolism and promotes metastases in triple-negative breast cancer. *Oncogene* 2017; **36:** 2116–2130.
112. Zhang W, Zhou P, Meng A, *et al*. Down-regulating Myoferlin inhibits the vasculogenic mimicry of melanoma via decreasing MMP-2 and inducing mesenchymal-to-epithelial transition. *J Cell Mol Med* 2018; **22:** 1743–1754.
113. Valli A, Rodriguez M, Moutsianas L, *et al*. Hypoxia induces a lipogenic cancer cell phenotype via HIF1α-dependent and -independent pathways. *Oncotarget* 2015; **6:** 1920–1941.
114. Dove DE, Su YR, Zhang W, *et al*. ACAT1 deficiency disrupts cholesterol efflux and alters cellular morphology in macrophages. *Arterioscler Thromb Vasc Biol* 2005; **25:** 128–134.
115. Krautbauer S, Haberl EM, Eisinger K, *et al*. Annexin A6 regulates adipocyte lipid storage and adiponectin release. *Mol Cell Endocrinol* 2017; **439:** 419–430.
116. Leca J, Martinez S, Lac S, *et al*. Cancer-associated fibroblast-derived annexin A6+ extracellular vesicles support pancreatic cancer aggressiveness. *J Clin Invest* 2016; **126:** 4140–4156.
117. Park JE, Dutta B, Tse SW, *et al*. Hypoxia-induced tumor exosomes promote M2-like macrophage polarization of infiltrating myeloid cells and microRNA-mediated metabolic shift. *Oncogene* 2019; **38:** 5158–5173.
118. Monastyrskaya K, Tschumi F, Babiychuk EB, *et al*. Annexins sense changes in intracellular pH during hypoxia. *Biochem J* 2008; **409:** 65–75.
119. Ikemori RY, Machado CM, Furuzawa KM, *et al*. Galectin-3 up-regulation in hypoxic and nutrient deprived microenvironments promotes cell survival. *PLoS One* 2014; **9:** e111592.
120. Cardoso AC, Andrade LN, Bustos SO, *et al*. Galectin-3 determines tumor cell adaptive strategies in stressed tumor microenvironments. *Front Oncol* 2016; **6:** 127.
121. Blasetti Fantauzzi C, Iacobini C, Menini S, *et al*. Galectin-3 gene deletion results in defective adipose tissue maturation and impaired insulin sensitivity and glucose homeostasis. *Sci Rep* 2020; **10:** 20070.
122. Jin GZ, Zhang Y, Cong WM, *et al*. Phosphoglucomutase 1 inhibits hepatocellular carcinoma progression by regulating glucose trafficking. *PLoS Biol* 2018; **16:** e2006483.
123. Cao B, Deng H, Cui H, *et al*. Knockdown of PGM1 enhances anticancer effects of orlistat in gastric cancer under glucose deprivation. *Cancer Cell Int* 2021; **21:** 481.
124. Loftus SK, Baxter LL, Cronin JC, *et al*. Hypoxia-induced HIF1α targets in melanocytes reveal a molecular profile associated with poor melanoma prognosis. *Pigment Cell Melanoma Res* 2017; **30:** 339–352.
125. Guo K, Lukacik P, Papagrigoriou E, *et al*. Characterization of human DHRS6, an orphan short chain dehydrogenase/reductase enzyme: a novel, cytosolic type 2 R-beta-hydroxybutyrate dehydrogenase. *J Biol Chem* 2006; **281:** 10291–10297.
126. Maurer GD, Brucker DP, Bähr O, *et al*. Differential utilization of ketone bodies by neurons and glioma cell lines: a rationale for ketogenic diet as experimental glioma therapy. *BMC Cancer* 2011; **11:** 315.
127. Dahl T, Ranheim T, Holm S, *et al*. Nicotinamide phosphoribosyltransferase and lipid accumulation in macrophages. *Eur J Clin Invest* 2011; **41:** 1098–1104.
128. Zhang LQ, Van Haandel L, Xiong M, *et al*. Metabolic and molecular insights into an essential role of nicotinamide phosphoribosyltransferase. *Cell Death Dis* 2017; **8:** e2705.
129. Audrito V, Messana VG, Deaglio S. NAMPT and NAPRT: two metabolic enzymes with key roles in inflammation. *Front Oncol* 2020; **10:** 358.
130. Grolla AA, Travelli C, Genazzani AA, *et al*. Extracellular nicotinamide phosphoribosyltransferase, a new cancer metabokine. *Br J Pharmacol* 2016; **173:** 2182–2194.
131. Grolla AA, Torretta S, Gnemmi I, *et al*. Nicotinamide phosphoribosyltransferase (NAMPT/PBEF/visfatin) is a tumoural cytokine released from melanoma. *Pigment Cell Melanoma Res* 2015; **28:** 718–729.
132. Röhrig F, Schulze A. The multifaceted roles of fatty acid synthesis in cancer. *Nat Rev Cancer* 2016; **16:** 732–749.
133. Fhu CW, Ali A. Fatty acid synthase: an emerging target in cancer. *Molecules* 2020: 25.
134. Lee CK, Jeong SH, Jang C, *et al*. Tumor metastasis to lymph nodes requires YAP-dependent metabolic adaptation. *Science* 2019; **363:** 644–649.
135. Zecchin KG, Rossato FA, Raposo HF, *et al*. Inhibition of fatty acid synthase in melanoma cells activates the intrinsic pathway of apoptosis. *Lab Invest* 2011; **91:** 232–240.
136. Seguin F, Carvalho MA, Bastos DC, *et al*. The fatty acid synthase inhibitor orlistat reduces experimental metastases and angiogenesis in B16-F10 melanomas. *Br J Cancer* 2012; **107:** 977–987.
137. Bastos DC, Paupert J, Maillard C, *et al*. Effects of fatty acid synthase inhibitors on lymphatic vessels: an in vitro and in vivo study in a melanoma model. *Lab Invest* 2017; **97:** 194–206.
138. Innocenzi D, Alò PL, Balzani A, *et al*. Fatty acid synthase expression in melanoma. *J Cutan Pathol* 2003; **30:** 23–28.
139. Du H, Wang Y, Zhang Z, *et al*. Fibronectin overexpression modulates formation of macrophage foam cells by activating SREBP2 involved in endoplasmic reticulum stress. *Cell Physiol Biochem* 2015; **36:** 1821–1834.
140. Page K, Lange Y. Cell adhesion to fibronectin regulates membrane lipid biosynthesis through 5'-AMP-activated protein kinase. *J Biol Chem* 1997; **272:** 19339–19342.
141. Wouters J, Stas M, Govaere O, *et al*. A novel hypoxia-associated subset of FN1 high MITF low melanoma cells: identification, characterization, and prognostic value. *Mod Pathol* 2014; **27:** 1088–1100.

142. Olbryt M, Habryka A, Tyszkiewicz T, *et al*. Melanoma-associated genes, MXI1, FN1, and NME1, are hypoxia responsive in murine and human melanoma cells. *Melanoma Res* 2011; **21:** 417–425.
143. Chen JC, Cai HY, Wang Y, *et al*. Up-regulation of stomatin expression by hypoxia and glucocorticoid stabilizes membrane-associated actin in alveolar epithelial cells. *J Cell Mol Med* 2013; **17:** 863–872.
144. Oh J, Kim CS, Kim M, *et al*. Type VI collagen and its cleavage product, endotrophin, cooperatively regulate the adipogenic and lipolytic capacity of adipocytes. *Metabolism* 2021; **114:** 154430.
145. Meri S, Haapasalo K. Function and dysfunction of complement factor H during formation of lipid-rich deposits. *Front Immunol* 2020; **11:** 611830.
146. Laskowski J, Renner B, Pickering MC, *et al*. Complement factor H-deficient mice develop spontaneous hepatic tumors. *J Clin Invest* 2020; **130:** 4039–4054.
147. Armento A, Honisch S, Panagiotakopoulou V, *et al*. Loss of complement factor H impairs antioxidant capacity and energy metabolism of human RPE cells. *Sci Rep* 2020; **10:** 10320.
148. Nuñez-Garcia M, Gomez-Santos B, Buqué X, *et al*. Osteopontin regulates the cross-talk between phosphatidylcholine and cholesterol metabolism in mouse liver. *J Lipid Res* 2017; **58:** 1903–1915.
149. Alza NP, Iglesias González PA, Conde MA, *et al*. Lipids at the crossroad of α-synuclein function and dysfunction: biological and pathological implications. *Front Cell Neurosci* 2019; **13:** 175.
150. Haeggström JZ. Leukotriene A4 hydrolase/aminopeptidase, the gatekeeper of chemotactic leukotriene B4 biosynthesis. *J Biol Chem* 2004; **279:** 50639–50642.
151. Zhu W, Zhou BL, Rong LJ, *et al*. Roles of PTBP1 in alternative splicing, glycolysis, and oncogensis. *J Zhejiang Univ Sci B* 2020; **21:** 122–136.
152. Kumar S, Gomez EC, Chalabi-Dchar M, *et al*. Integrated analysis of mRNA and miRNA expression in HeLa cells expressing low levels of Nucleolin. *Sci Rep* 2017; **7:** 9017.
153. Tian N, Liu Q, Li Y, *et al*. Transketolase deficiency in adipose tissues protects mice from diet-induced obesity by promoting lipolysis. *Diabetes* 2020; **69:** 1355–1367.
154. Jannapureddy S, Sharma M, Yepuri G, *et al*. Aldose reductase: an emerging target for development of interventions for diabetic cardiovascular complications. *Front Endocrinol (Lausanne)* 2021; **12:** 636267.
155. Shan Y, Yang G, Huang H, *et al*. Ubiquitin-like modifier activating enzyme 1 as a novel diagnostic and prognostic indicator that correlates with ferroptosis and the malignant phenotypes of liver cancer cells. *Front Oncol* 2020; **10:** 592413.
156. Krautbauer S, Neumeier M, Rein-Fischboeck L, *et al*. Adipocyte hypertrophy and improved postprandial lipid response in beta 2 syntrophin deficient mice. *Cell Physiol Biochem* 2019; **52:** 1151–1165.
157. Hebel T, Eisinger K, Neumeier M, *et al*. Lipid abnormalities in alpha/beta2-syntrophin null mice are independent from ABCA1. *Biochim Biophys Acta* 2015; **1851:** 527–536.
158. Kim EY, Kim WK, Kang HJ, *et al*. Acetylation of malate dehydrogenase 1 promotes adipogenic differentiation via activating its enzymatic activity. *J Lipid Res* 2012; **53:** 1864–1876.
159. Li J, Huang Q, Long X, *et al*. CD147 reprograms fatty acid metabolism in hepatocellular carcinoma cells through Akt/mTOR/SREBP1c and P38/PPARα pathways. *J Hepatol* 2015; **63:** 1378–1389.
160. Serini G, Tamagnone L. Bad vessels beware! Semaphorins will sort you out! *EMBO Mol Med* 2015; **7:** 1251–1253.
161. Valentini E, Di Martile M, Del Bufalo D, *et al*. SEMAPHORINS and their receptors: focus on the crosstalk between melanoma and hypoxia. *J Exp Clin Cancer Res* 2021; **40:** 131.
162. Mejhert N, Wilfling F, Esteve D, *et al*. Semaphorin 3C is a novel adipokine linked to extracellular matrix composition. *Diabetologia* 2013; **56:** 1792–1801.
163. Pursiheimo JP, Rantanen K, Heikkinen PT, *et al*. Hypoxia-activated autophagy accelerates degradation of SQSTM1/p62. *Oncogene* 2009; **28:** 334–344.
164. Rantanen K, Pursiheimo JP, Högel H, *et al*. p62/SQSTM1 regulates cellular oxygen sensing by attenuating PHD3 activity through aggregate sequestration and enhanced degradation. *J Cell Sci* 2013; **126:** 1144–1154.
165. König K, Marth L, Roissant J, *et al*. The plexin C1 receptor promotes acute inflammation. *Eur J Immunol* 2014; **44:** 2648–2658.
166. Morote-Garcia JC, Napiwotzky D, Köhler D, *et al*. Endothelial Semaphorin 7A promotes neutrophil migration during hypoxia. *Proc Natl Acad Sci U S A* 2012; **109:** 14146–14151.
167. Park JE, Tan HS, Datta A, *et al*. Hypoxic tumor cell modulates its microenvironment to enhance angiogenic and metastatic potential by secretion of proteins and exosomes. *Mol Cell Proteomics* 2010; **9:** 1085–1099.
168. Chu K, Boley KM, Moraes R, *et al*. The paradox of E-cadherin: role in response to hypoxia in the tumor microenvironment and regulation of energy metabolism. *Oncotarget* 2013; **4:** 446–462.
169. Xu C, Gu L, Kuerbanjiang M, *et al*. Thrombospondin 2/toll-like receptor 4 axis contributes to HIF-1α-derived glycolysis in colorectal cancer. *Front Oncol* 2020; **10:** 557730.
170. MacLauchlan SC, Calabro NE, Huang Y, *et al*. HIF-1α represses the expression of the angiogenesis inhibitor thrombospondin-2. *Matrix Biol* 2018; **65:** 45–58.
171. Schietke R, Warnecke C, Wacker I, *et al*. The lysyl oxidases LOX and LOXL2 are necessary and sufficient to repress E-cadherin in hypoxia: insights into cellular transformation processes mediated by HIF-1. *J Biol Chem* 2010; **285:** 6658–6669.
172. Asplund A, Stillemark-Billton P, Larsson E, *et al*. Hypoxic regulation of secreted proteoglycans in macrophages. *Glycobiology* 2010; **20:** 33–40.
173. Wight TN, Kang I, Evanko SP, *et al*. Versican-A critical extracellular matrix regulator of immunity and inflammation. *Front Immunol* 2020; **11:** 512.
174. Touab M, Villena J, Barranco C, *et al*. Versican is differentially expressed in human melanoma and may play a role in tumor development. *Am J Pathol* 2002; **160:** 549–557.
175. Zheng H, Wu Y, Guo T, *et al*. Hypoxia induces growth differentiation factor 15 to promote the metastasis of colorectal cancer via PERK-eIF2. *Biomed Res Int* 2020; **2020:** 5958272.
176. Schelter F, Halbgewachs B, Bäumler P, *et al*. Tissue inhibitor of metalloproteinases-1-induced scattered liver metastasis is mediated by hypoxia-inducible factor-1α. *Clin Exp Metastasis* 2011; **28:** 91–99.
177. Turnberg D, Botto M, Lewis M, *et al*. CD59a deficiency exacerbates ischemia-reperfusion injury in mice. *Am J Pathol* 2004; **165:** 825–832.
178. Zhang C, Lu L, Li Y, *et al*. IGF binding protein-6 expression in vascular endothelial cells is induced by hypoxia and plays a negative role in tumor angiogenesis. *Int J Cancer* 2012; **130:** 2003–2012.
179. Coma S, Shimizu A, Klagsbrun M. Hypoxia induces tumor and endothelial cell migration in a semaphorin 3F- and VEGF-dependent manner via transcriptional repression of their common receptor neuropilin 2. *Cell Adh Migr* 2011; **5:** 266–275.
180. Soni H, Bode J, Nguyen CDL, *et al*. PERK-mediated expression of peptidylglycine α-amidating monooxygenase supports angiogenesis in glioblastoma. *Oncogenesis* 2020; **9:** 18.
181. Yao X, Ping Y, Liu Y, *et al*. Vascular endothelial growth factor receptor 2 (VEGFR-2) plays a key role in vasculogenic mimicry formation, neovascularization and tumor initiation by Glioma stem-like cells. *PLoS One* 2013; **8:** e57188.
182. Hendrix MJ, Seftor EA, Hess AR, *et al*. Vasculogenic mimicry and tumour-cell plasticity: lessons from melanoma. *Nat Rev Cancer* 2003; **3:** 411–421.

183. Maniotis AJ, Folberg R, Hess A, *et al*. Vascular channel formation by human melanoma cells in vivo and in vitro: vasculogenic mimicry. *Am J Pathol* 1999; **155:** 739–752.
184. Seftor RE, Hess AR, Seftor EA, *et al*. Tumor cell vasculogenic mimicry: from controversy to therapeutic promise. *Am J Pathol* 2012; **181:** 1115–1125.
185. Tse SW, Tan CF, Park JE, *et al*. Microenvironmental hypoxia induces dynamic changes in lung cancer synthesis and secretion of extracellular vesicles. *Cancers (Basel)* 2020: 12.
186. Goddi A, Carmona A, Schroedl L, *et al*. Laminin-α4 is upregulated in both human and murine models of obesity. *Front Endocrinol (Lausanne)* 2021; **12:** 698621.
187. Larson AR, Lee CW, Lezcano C, *et al*. Melanoma spheroid formation involves laminin-associated vasculogenic mimicry. *Am J Pathol* 2014; **184:** 71–78.
188. Young A, Mittal D, Stagg J, *et al*. Targeting cancer-derived adenosine: new therapeutic approaches. *Cancer Discov* 2014; **4:** 879–888.
189. Yu M, Guo G, Huang L, *et al*. CD73 on cancer-associated fibroblasts enhanced by the A. *Nat Commun* 2020; **11:** 515.
190. Chambers AM, Matosevic S. Immunometabolic dysfunction of natural killer cells mediated by the hypoxia-CD73 axis in solid tumors. *Front Mol Biosci* 2019; **6:** 60.
191. Wang J, Ding N, Li Y, *et al*. Insulin-like growth factor binding protein 5 (IGFBP5) functions as a tumor suppressor in human melanoma cells. *Oncotarget* 2015; **6:** 20636–20649.
192. Johansson E, Grassi ES, Pantazopoulou V, *et al*. CD44 interacts with HIF-2α to modulate the hypoxic phenotype of perinecrotic and perivascular glioma cells. *Cell Rep* 2017; **20:** 1641–1653.
193. Luo B, Lee AS. The critical roles of endoplasmic reticulum chaperones and unfolded protein response in tumorigenesis and anticancer therapies. *Oncogene* 2013; **32:** 805–818.
194. Asplund A, Ostergren-Lundén G, Camejo G, *et al*. Hypoxia increases macrophage motility, possibly by decreasing the heparan sulfate proteoglycan biosynthesis. *J Leukoc Biol* 2009; **86:** 381–388.
195. Chawsheen HA, Ying Q, Jiang H, *et al*. A critical role of the thioredoxin domain containing protein 5 (TXNDC5) in redox homeostasis and cancer development. *Genes Dis* 2018; **5:** 312–322.
196. Feldser D, Agani F, Iyer NV, *et al*. Reciprocal positive regulation of hypoxia-inducible factor 1alpha and insulin-like growth factor 2. *Cancer Res* 1999; **59:** 3915–3918.
197. Sibenaller ZA, Welsh JL, Du C, *et al*. Extracellular superoxide dismutase suppresses hypoxia-inducible factor-1α in pancreatic cancer. *Free Radic Biol Med* 2014; **69:** 357–366.
198. Yang Z, Zhang C, Feng Y, *et al*. Tenascin-C is involved in promotion of cancer stemness via the Akt/HIF1α axis in esophageal squamous cell carcinoma. *Exp Mol Pathol* 2019; **109:** 104239.
199. Spenlé C, Saupe F, Midwood K, *et al*. Tenascin-C: exploitation and collateral damage in cancer management. *Cell Adh Migr* 2015; **9:** 141–153.
200. Kim JH, Park MY, Kim CN, *et al*. Expression of endothelial cell-specific molecule-1 regulated by hypoxia inducible factor-1α in human colon carcinoma: impact of ESM-1 on prognosis and its correlation with clinicopathological features. *Oncol Rep* 2012; **28:** 1701–1708.
201. Xiao W, Wang X, Wang T, *et al*. Overexpression of BMP1 reflects poor prognosis in clear cell renal cell carcinoma. *Cancer Gene Ther* 2020; **27:** 330–340.
202. Takahashi H, Katsuta E, Yan L, *et al*. High expression of Annexin A2 is associated with DNA repair, metabolic alteration, and worse survival in pancreatic ductal adenocarcinoma. *Surgery* 2019; **166:** 150–156.
203. Jiang S, Xu Y. Annexin A2 upregulation protects human retinal endothelial cells from oxygen-glucose deprivation injury by activating autophagy. *Exp Ther Med* 2019; **18:** 2901–2908.
204. Biaoxue R, Xiguang C, Hua L, *et al*. Stathmin-dependent molecular targeting therapy for malignant tumor: the latest 5 years' discoveries and developments. *J Transl Med* 2016; **14:** 279.
205. Cecconi D, Carbonare LD, Mori A, *et al*. An integrated approach identifies new oncotargets in melanoma. *Oncotarget* 2018; **9:** 11489–11502.
206. Han N, Li W, Zhang M. The function of the RNA-binding protein hnRNP in cancer metastasis. *J Cancer Res Ther* 2013; **9:** S129–S134.
207. Xu H, Rahimpour S, Nesvick CL, *et al*. Activation of hypoxia signaling induces phenotypic transformation of glioma cells: implications for bevacizumab antiangiogenic therapy. *Oncotarget* 2015; **6:** 11882–11893.
208. Zheng X, Zhou AX, Rouhi P, *et al*. Hypoxia-induced and calpain-dependent cleavage of filamin A regulates the hypoxic response. *Proc Natl Acad Sci U S A* 2014; **111:** 2560–2565.
209. Storr SJ, Thompson N, Pu X, *et al*. Calpain in breast cancer: role in disease progression and treatment response. *Pathobiology* 2015; **82:** 133–141.
210. Kuo TF, Chen TY, Jiang ST, *et al*. Protein disulfide isomerase a4 acts as a novel regulator of cancer growth through the procaspase pathway. *Oncogene* 2017; **36:** 5484–5496.
211. Albakova Z, Armeev GA, Kanevskiy LM, *et al*. HSP70 multifunctionality in cancer. *Cells* 2020: 9.
212. Dang DT, Chun SY, Burkitt K, *et al*. Hypoxia-inducible factor-1 target genes as indicators of tumor vessel response to vascular endothelial growth factor inhibition. *Cancer Res* 2008; **68:** 1872–1880.
213. Alles SRA, Gomez K, Moutal A, *et al*. Putative roles of SLC7A5 (LAT1) transporter in pain. *Neurobiol Pain* 2020; **8:** 100050.
214. Onishi Y, Hiraiwa M, Kamada H, *et al*. Hypoxia affects Slc7a5 expression through HIF-2α in differentiated neuronal cells. *FEBS Open Bio* 2019; **9:** 241–247.
215. Zhang Y, Cai H, Liao Y, *et al*. Activation of PGK1 under hypoxic conditions promotes glycolysis and increases stem cell-like properties and the epithelial-mesenchymal transition in oral squamous cell carcinoma cells via the AKT signalling pathway. *Int J Oncol* 2020; **57:** 743–755.
216. Jiang H, Cheng XW, Shi GP, *et al*. Cathepsin K-mediated Notch1 activation contributes to neovascularization in response to hypoxia. *Nat Commun* 2014; **5:** 3838.
217. Li X, Hattori A, Takahashi S, *et al*. Ubiquitin carboxyl-terminal hydrolase L1 promotes hypoxia-inducible factor 1-dependent tumor cell malignancy in spheroid models. *Cancer Sci* 2020; **111:** 239–252.
218. Jiang X, Zhang S, Yin Z, *et al*. The correlation between NEDD4L and HIF-1α levels as a gastric cancer prognostic marker. *Int J Med Sci* 2019; **16:** 1517–1524.
219. Soumoy L, Kindt N, Ghanem G, *et al*. Role of macrophage migration inhibitory factor (MIF) in melanoma. *Cancers (Basel)* 2019: 11.
220. Oda S, Oda T, Nishi K, *et al*. Macrophage migration inhibitory factor activates hypoxia-inducible factor in a p53-dependent manner. *PLoS One* 2008; **3:** e2215.
221. Chen Y, Wu YR, Yang HY, *et al*. Prolyl isomerase Pin1: a promoter of cancer and a target for therapy. *Cell Death Dis* 2018; **9:** 883.

References 88–221 are cited only in the supplementary material.

SUPPLEMENTARY MATERIAL ONLINE

Figure S1. Adipophilin expression correlation with chromosome 3 copy number and age

Figure S2. Adipophilin expression correlation with different genomic and clinical variables

Figure S3. RT-qPCR and viability assay results

Table S1. LOORG pUM ($n = 14$) secretome protein list, including max fold-change and clinical scores

Table S2. Immune metabolism categories with respective reference numbers. GDC-TCGA-UM gene variance levels (in decimal units)

Table S3. Kaplan–Meier p value scores of good- and poor-survival predicting genes from GDC-TCGA-UM cohort

Table S4. Primer sequences used for qPCR